RIJKSUNIVERSITEIT GRONINGEN - JULY 1, 2024

# Exploring Antioxidants: OBE100 Extract and Nanodiamond-Based Quantum Sensing for Tissue Analysis

*Author:*
Patricija K. OZOLINA
*(S4858387)*

*Supervisor:*
Prof./ Dr. Romana SCHIRHAGL
*Second examiner :*
Dr. Claudia REYES SAN MARTIN
*Daily Supervisor:*
Elkin L. ESCOBAR CHAVES

**UMCG**  **BBT** BIOMATERIALS AND BIOMEDICAL TECHNOLOGY

BACHELOR'S THESIS: TO FULFILL THE REQUIREMENTS
FOR A BACHELOR'S IN BIOMEDICAL ENGINEERING AT THE UNIVERSITY OF GRONINGEN

# Abstract

Aging and hepatic steatosis are prevalent conditions associated with oxidative stress, for which effective treatments are urgently needed. This study investigates OBE100, an extract from *Eucalyptus tereticornis* leaves, for its antioxidant potential in combating free radicals in liver tissue. Precision-cut liver slices from mouse models of aging, hepatic steatosis, and control animals are used in this effort. Additionally, it explores the application of nanodiamond-based quantum sensing for assessing free radicals in tissues and aims to refine this methodology by enhancing the understanding of fluorescent nanodiamond distribution within tissues.

OBE100 demonstrates robust antioxidant potential; however, its onset of action is delayed and necessitates additional dosing. In models of hepatic steatosis, OBE100 effectively restores free radical levels to their pre-steatotic state, and this effect coincides with its hypolipemic activity. Viability assays also reveal no detrimental effects of OBE100 on precision-cut liver slice health. Thus, OBE100 emerges as a promising candidate for managing oxidative stress associated with steatotic liver disease and aging—two conditions urgently requiring effective treatments.

Furthermore, this research demonstrates that nanodiamond-based quantum sensing can effectively assess free radical generation in tissue slices, representing a novel achievement.

# Contents

## 4   Discussion     34

# Acronyms

**AFLD** alcoholic fatty liver disease

**ANOVA** analysis of variance

**ATP** adenosine triphosphate

**BSA** bovine serum albumin

**CI** confidence interval

**DMEM** Dulbecco's Modified Eagle Medium

**DMSO** dimethyl sulfoxide

**DNA** deoxyribonucleic acid

**ECM** extracellular matrix

**Eu** Eucalyptus tereticornis

**FACS** Fluorescence-activated cell sorting

**FFA** free fatty acids

**FND** fluorescent nanodiamond

**MQ water** Milli-Q water

**NAFLD** nonalcoholic fatty liver disease

**NaOH** sodium hydroxide

**NV** nitrogen-vacancy

**PBS** phosphate-buffered saline

**PCLS** precision-cut liver slices

**PCS** precision-cut slices

**RMS** reactive molecular species

**RNA** ribonucleic acid

**RNS** reactive nitrogen species

**ROS** reactive oxygen species

**SH** steatohepatitis

**SONOP** sonification solution

**T1** spin-lattice relaxation time

**TBS** TRIS-buffered saline

**UW** University of Wisconsin

**WEGG** William's E Glucose Gentamicin

# 1 Introduction

Reactive molecular species (RMS) are short-lived molecules known for their propensity to react with biological materials (Wolfle et al., 2014). They are classified based on their elemental origins (e.g., oxygen, nitrogen) and the presence of unpaired free electrons (paramagnetic free radicals or non-paramagnetic molecules) (Damle et al., 2022) (Figure 1).
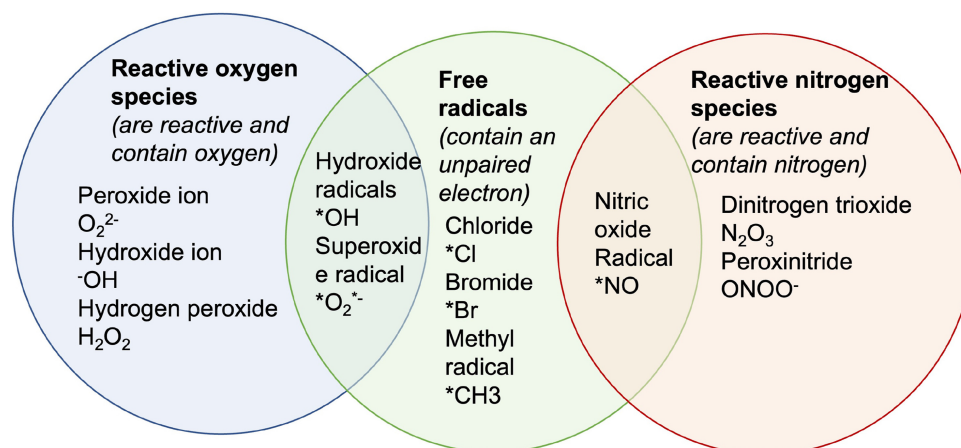


**Reactive oxygen species**
*(are reactive and contain oxygen)*

Peroxide ion
$O_2^{2-}$
Hydroxide ion
$^-OH$
Hydrogen peroxide
$H_2O_2$

Hydroxide radicals
$^*OH$
Superoxide radical
$^*O_2^{*-}$

**Free radicals**
*(contain an unpaired electron)*
Chloride
$^*Cl$
Bromide
$^*Br$
Methyl radical
$^*CH3$

Nitric oxide Radical
$^*NO$

**Reactive nitrogen species**
*(are reactive and contain nitrogen)*

Dinitrogen trioxide
$N_2O_3$
Peroxinitride
$ONOO^-$

**Figure 1.** Illustration of the division of RMS with corresponding examples for each category (Damle et al., 2022)

Free radicals, a subset of RMS, harbor free electrons in their outer shell and serve as indispensable entities in numerous aspects of everyday existence (Phaniendra et al., 2014). Derived as inherent byproducts of cellular metabolism, their involvement permeates diverse physiological and cellular functions, encompassing immune defenses (Knight, 2000), cellular signaling pathways (Bokkon, 2012), and responses to external stimuli such as environmental pollution, tobacco smoke, electromagnetic radiation, and specific pharmaceutical agents (Lobo et al., 2010).

Free radicals encompass certain members of reactive oxygen species (ROS) and reactive nitrogen species (RNS). ROS comprise oxygen-containing molecules generated from disruptions in electron flow along the respiratory chain. These disruptions lead to the production of intermediates that subsequently interact with oxygen, resulting in the formation of ROS. Additionally, ROS can be produced in response to cellular reactions to xenobiotics, cytokines, and bacterial invasion (Ray et al., 2012; Smirne et al., 2022). RNS, nitrogen-based compounds associated with oxygen, result from the interaction of nitric oxide with ROS (Alhasawi et al., 2019; Jakubczyk et al., 2020; Y. R. Li & Trush, 2016).

Free radicals are typically regulated by the body's natural mechanisms. However, an excessive accumulation, surpassing the body's capacity for gradual neutralization using antioxidant defenses, leads to oxidative stress. The primary contributors to this phenotype include elevated production of ROS and impaired antioxidant systems (Martinez-Reyes & Cuezva, 2014). Oxidative stress induces direct or indirect damage to nucleic acids, proteins, and lipids, thereby contributing to the pathogenesis of various chronic and degenerative diseases, including carcinogenesis, neurodegeneration, atherosclerosis, diabetes, and aging (Ray et al., 2012). The study reported delves into the ramifications of reducing free radicals in two conditions associated with oxidative stress: aging and steatotic liver disease.

Aging encompasses the gradual and progressive decline in cellular and organ functions over time, resulting in increased vulnerability to chronic diseases and mortality in living organisms (Srivastava, 2017). Apart from individual implications, it has far-reaching societal effects, spanning economic and healthcare domains. With an aging population, there is a heightened demand for healthcare services to address age-related ailments, resulting in increased societal healthcare expenses (Institute of Medicine (US) Committee on the Future Health Care Workforce for Older Americans, 2008). These intertwined consequences underscore the complexity of aging and stress the necessity for approaches to comprehend and tackle this biological phenomenon.

There is a tight link between ROS generation and oxidative damage during aging. A peer-reviewed study by Lopez-Otin et al. (2013) identified nine hallmark features of aging, which were later updated to twelve (Lopez-Otin et al., 2023). These hallmarks have continuously evolved to reflect the latest discoveries and are now widely accepted as a common standard within the research community. Among them is mitochondrial dysfunction, which is closely associated with ROS production during oxidative phosphorylation (Lopez-Otin et al., 2016; Warraich et al., 2020). Mitochondria play pivotal roles in myriad cellular functions, including metabolism, signal transduction, ion homeostasis, oxidative stress, and programmed cell death pathways. Any disruption in mitochondrial activity can significantly impact cell viability and function (Srivastava, 2017).

As individuals age, mitochondrial function declines through various mechanisms, including the accumulation of mutations in mitochondrial deoxyribonucleic acid (DNA), impaired proteostasis leading to the destabilization of respiratory chain complexes, decreased turnover of mitochondria, and alterations in mitochondrial dynamics (Srivastava, 2017). This deterioration compromises the role of mitochondria in cellular bioenergetics, increases the generation of ROS, and can provoke accidental permeabilization of mitochondrial membranes, resulting in inflammation and cell death (Lopez-Otin et al., 2023).

ROS is also pivotal in mitophagy, a specialized form of autophagy that selectively eliminates surplus or damaged mitochondria. However, as individuals age, there is a reduction in both mitophagy and autophagy pathways, associated with numerous age-related conditions including neurodegenerative diseases, cardiac complications, immune system disorders, hepatic and renal dysfunction, and cancer. This decline leads to impaired mitochondrial function, ultimately resulting in elevated ROS production (Srivastava, 2017).

Steatotic liver disease is the most prevalent chronic liver condition, impacting over a quarter of the global population (Kokkorakis et al., 2024). It is characterized by hepatic steatosis, the excessive accumulation of triglycerides within hepatocytes, the main parenchymal cells of the liver (Z. Zhou et al., 2015). This condition is primarily associated with two major metabolic disorders: nonalcoholic fatty liver disease (NAFLD) and alcoholic fatty liver disease (AFLD) (Idilman et al., 2016). AFLD is associated with a history of excessive drinking, typically described as exceeding 14 standard drinks per week for women and 21 for men; NAFLD is not linked to alcohol consumption (Smirne et al., 2022). NAFLD and AFLD represent significant global health concerns, with their prevalence increasing steadily. NAFLD affects approximately 23-25% of the general adult population, with the highest rates observed in the Middle East (32%) and South America (30%), and the lowest in Africa (13%) (Lazarus et al., 2021). Furthermore, this condition is closely linked to the global increase in obesity (Fabbrini et al., 2009; Loomba & Sanyal, 2013). AFLD, on the other hand, is estimated to affect about 4.3-4.7% of the population (Wong et al., 2019). Both conditions manifest across a spectrum of pathologies, ranging from simple steatosis to steatohepatitis (SH), characterized by inflammation of the

liver tissue, cirrhosis, and even hepatocellular carcinoma (Singh et al., 2017).

Hepatic steatosis primarily stems from increased uptake, decreased export, or impaired breakdown of free fatty acids (FFA). When macronutrient intake exceeds immediate energy needs, the liver converts unused carbohydrates and proteins into triglycerides for storage. Subsequently, during periods of reduced intake or increased energy expenditure, these stored lipids are mobilized and utilized (Smirne et al., 2022).

Over time, the liver loses its capacity to adaptively compensate for the accumulation of fatty acids within hepatocytes, as the increase in mitochondrial respiration becomes bioenergetically inefficient. This results in structural and functional changes in mitochondria, marking the initiation of NAFLD or AFLD (Meex & Blaak, 2020; Rabelo et al., 2024).

Hepatocytes in hepatic steatosis attempt to mitigate lipid excess by upregulating fat oxidation within microsomes and peroxisomes (Smirne et al., 2022). However, the process of reoxidizing NADH to NAD+ within mitochondria is linked to electron leakage from the mitochondrial respiratory chain, leading to enhanced ROS generation and elevated oxidative stress levels (Rabelo et al., 2024).

Impaired redox status and subsequent accumulation of ROS are implicated as the primary drivers of hepatic maladaptive responses to fat accumulation, resulting in metabolic impairment and the progression to SH (Arroyave-Ospina et al., 2021). ROS can inhibit the hepatic secretion of very-low-density lipoproteins, exacerbating intrahepatic lipid accumulation and contributing to mitochondrial dysfunction in hepatocytes (Gambino et al., 2011). Moreover, the shift to beta-oxidation of FFA - the process by which fatty acids are broken down to produce energy (Talley & Mohiuddin, 2023) - observed in SH, exacerbates free radical production, leading to hepatocellular damage, inflammation, and eventual fibrosis through the activation of hepatic stellate cells (Sanyal et al., 2001). Furthermore, during liver injury, oxidative stress triggers the activation of redox-sensitive transcription factors, initiating an inflammatory response and activating cell death pathways in hepatocytes (Rabelo et al., 2024; Smirne et al., 2022).

Beyond lifestyle interventions aimed at weight loss, several drugs on the market target conditions associated with steatotic liver disease. These include medications that lower cholesterol or triglycerides, control blood pressure, or manage diabetes. However, many drug candidates have shown limited efficacy or failed in clinical trials, highlighting an urgent need for effective treatments (Kokkorakis et al., 2024). Therefore, the exploration of new drug candidates for steatotic liver diseases remains an active area of research.

Antioxidants play a pivotal role in mitigating the detrimental effects of free radicals by donating electrons and effectively neutralizing their impact. Studies have demonstrated that decreasing ROS levels or limiting their production rate can mitigate oxidative damage (Houldsworth, 2023). Lobo et al. (2010) suggested that this approach could delay aging, while Chen et al. (2020) and Sabir et al. (2022) proposed it might also limit the progression of steatotic liver disease.

*Eucalyptus tereticornis (Eu)* is renowned for its antioxidant properties. In a study by Acin et al. (2021), the Eu leaf extract OBE100, containing three pentacyclic triterpenes, demonstrated the ability to modulate immuno-metabolic activities associated with obesity and insulin resistance - two conditions exacerbated by oxidative stress. Furthermore, OBE100 exhibits anti-inflammatory properties, which are closely intertwined with oxidative stress, as chronic inflammation can contribute to the generation of free radicals (Acin et al., 2021; Smina et al., 2011; Yadav et al., 2010). Additionally, OBE100 has shown hypoglycemic and hypolipidemic

effects (Bentancur et al., 2021).

This research aims to evaluate the antioxidant efficacy of the OBE100 extract. The research question addressed is: *What impact does OBE100 have on free radicals in precision-cut liver slices (PCLS) obtained from naturally aged, fatty acid-induced, and positive control mice models?*

While in vitro models of human liver disease often lack the complexity of native liver architecture, PCLS maintain this intricate physiological structure, encompassing all liver cell types. This characteristic is vital for studying multifaceted liver functions and responses to toxic compounds in vitro, rendering PCLS an invaluable choice for this project (I. A. de Graaf et al., 2010; Dewyse et al., 2021).

Conventional methods for assessing oxidative stress and free radicals encompass both direct and indirect approaches. Direct measurements involve detecting cellular levels of ROS using probes, such as fluorogenic ones, and correlating fluorescence or absorbance with their concentrations. However, these techniques are challenged by issues related to selectivity, quantification, linearity of response, and susceptibility to artifacts (Murphy et al., 2022). Indirect methods evaluate oxidative damage to cellular components like lipids, proteins, and nucleic acids. For example, protein carbonyl content indicates protein damage (Levine et al., 1990), while lipid peroxidation levels estimate malondialdehyde content; immunohistochemical examination targets primary DNA lesions like thymidine glycol and can be used to assess nucleic acid damage. Nevertheless, these methods provide no spatial resolution and are destructive. Additionally, antioxidant levels and activity correlate with oxidative stress severity. Cellular responses are studied through changes in protein and ribonucleic acid (RNA) expression using techniques like quantitative polymerase chain reaction, RNA sequencing, or Western blotting (Katerji et al., 2019). However, these approaches are specific to certain radicals and do not provide spatial and temporal information on free radical responses. Magnetic resonance techniques, including nuclear magnetic resonance, electron spin resonance, and magnetic resonance imaging, show promise for detecting radicals by identifying their free electrons. Nonetheless, they possess limited sensitivity. (Damle et al., 2022; Dikalov & Harrison, 2014; Wu et al., 2022).

Nanodiamond-based quantum sensing is a novel technique that has recently emerged for evaluating oxidative stress and free radicals, and this method has undergone further refinement within the context of this research and its broader project. It addresses the common limitations of conventional methods used to assess oxidative stress, notably the difficulty of simultaneously localizing, quantifying, and identifying free radicals. Ultimately, it enables a detailed and nuanced understanding of free radical presence and behavior within a given system (Wu et al., 2022).

Nanodiamond-based quantum sensing utilizes fluorescent nanodiamonds (FNDs) containing lattice defects known as nitrogen-vacancy (NV) centers. The NV centers, arising from the replacement of a carbon atom by a nitrogen atom with an adjacent vacancy, impart optical and magnetic properties to the diamond. These unique properties enable NV centers to optically detect magnetic resonances by altering their brightness in response to the magnetic environment. The uptake of FNDs by cells mainly occurs through phagocytosis and endocytosis (Mzyk et al., 2022; Niora et al., 2023; Perona Martinez, 2020; Prabhakar et al., 2017; Y. Zhang, 2023).

Under normal conditions, the electronic spins within the NV center can be excited to the bright $m_s = 0$ state using a green laser. Upon deactivation of the laser, the electron spin states undergo repolarization, returning to the equilibrium between the $m_s = 0$ and $m_s = \pm 1$ states (Figure

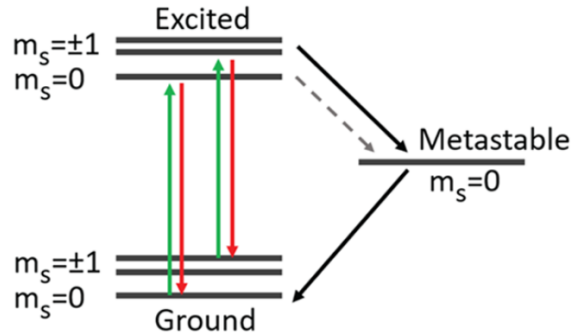2). The duration needed for this process is referred to as the spin-lattice relaxation time (T1) (Mzyk et al., 2022).



**Figure 2.** A diagram representing the energy levels of NV centers (Mzyk et al., 2022)

The brightness disparity between the $m_s = 0$ and $m_s = \pm 1$ states facilitates the optical monitoring of the transition and determination of its rate. By measuring the duration of the repolarization, varying concentrations of paramagnetic species, such as free radicals, can be detected. Higher concentrations of free radicals near the FND probe result in more unpaired electrons, accelerating the duration of the repolarization, and leading to a shorter relaxation time and a smaller T1 value. Conversely, lower concentrations of free radicals result in a longer relaxation time, leading to an increased T1 value (Figure 3) (Mzyk et al., 2022; Perona Martinez et al., 2020; Rondin et al., 2014).
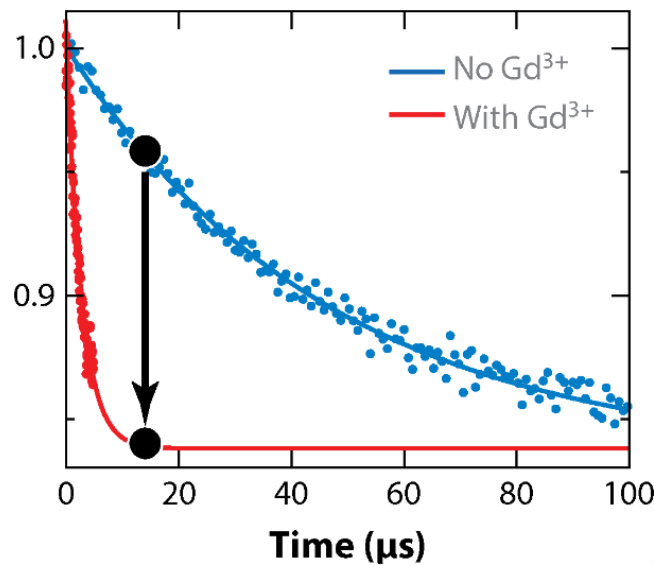


**Figure 3.** A diagram depicting the T1 relaxation curve of an NV center in the presence and absence of a paramagnetic species ($GdCl_3$ salt) (Schirhagl et al., 2014)

The primary hypothesis of this research proposes that OBE100 will significantly decrease free radicals, as indicated by elevated T1 values, following incubation periods of 6, 24, and 48 hours in precision-cut liver slices obtained from a naturally aged mouse model and a young model mimicking steatosis, along with a positive control group for the latter. This reduction will be assessed through a one-way analysis of variance (ANOVA) test, followed by Tukey's multiple comparison test with a 95% confidence interval (CI), comparing baseline measurements to those after incubation with the extract. Consequently, OBE100 is hypothesized to hold the

potential as a treatment for aging and steatotic liver disease by minimizing oxidative stress and its associated effects.

While the efficacy of nanodiamond-based quantum sensing in detecting free radicals within cells was established in 2021 (Sharmin et al., 2021), its feasibility in free radical detection within tissues remains unsubstantiated. Tissues present a more complex and physiologically relevant environment compared to isolated cells, offering functional integration that better mimics the organism (Abbott & Kaplan, 2015). Therefore, this research aims to explore the potential of nanodiamond-based quantum sensing for detecting free radicals in tissues and refine the methodology by improving our understanding of FND distribution within them, thereby significantly enhancing tissue-based methodologies.

The research question addressed in this part of the project is: *Can the application of nanodiamond-based quantum sensing offer an effective and feasible method for detecting free radicals in precision-cut slices (PCS) of the liver, heart, spleen, and kidney obtained from a naturally aged mouse model?*

Cellular uptake of FNDs can be determined by utilizing confocal microscopy to visualize FNDs in tissues undergoing Fluorescence-activated cell sorting (FACS).

FACS, a flow cytometry technique, is preferred when high purity of the target population is necessary and can be used when the identifying marker is expressed at low levels or when differential marker density is used for cell separation. It is the sole method for isolating cells based on intracellular protein expression or internal staining. FACS enables the purification of individual cells based on size, granularity, and fluorescence (Basu et al., 2010).

To isolate cells of interest, they are initially labeled with fluorescently-tagged monoclonal antibodies recognizing specific surface markers; negative selection of unstained cells is also feasible (Herzenberg et al., 2000). During FACS, cells in suspension are passed as droplets, each containing a single cell, in front of a laser. The fluorescence detection system identifies cells of interest based on predetermined parameters, and the instrument charges and sorts them accordingly into collection tubes using an electrostatic deflection system (Basu et al., 2010; Longobardi Givan, 2001).

Confocal microscopy, a technique in light microscopy used for imaging fluorescently labeled specimens, operates by sequentially illuminating a specific region of the sample. This illumination is achieved by scanning focused light beams from a laser across the specimen and using a pinhole to exclude extraneous light from reaching the detector (Paddock & Eliceiri, 2013). This process enables the confocal microscope to produce clear images of the specimen that would otherwise appear blurred under standard light microscopy. These images exhibit less haze and improved contrast compared to those obtained with conventional techniques, presenting a thin cross-section of the specimen. Additionally, confocal microscopy enables the construction of three-dimensional reconstructions by compiling a series of thin slices taken along the vertical axis (Semwogerere & Weeks, 2008).

# 2 Materials and Methods

## 2.1 Fluorescent Nanodiamonds

The research employed ground HPHT diamonds (ND-NV-120nm) sourced from Adamas Nanotechnology. The manufacturer subjected the diamonds to irradiation using 3 MeV electrons at a fluence of $5 \times 10^{19}\,\mathrm{cm}^{-2}$. This process created vacancies within the diamonds, which became mobile during annealing at temperatures exceeding 600 °C. The vacancies were combined with nitrogen atoms to form NV centers. Following irradiation, the particles underwent cleaning with oxidizing acid, resulting in oxygen-terminated surfaces (Shenderova et al., 2019). Previous experiments validated the suitability of this particle size for the intended application (Sigaeva et al., 2022). These particles have been extensively utilized for diverse purposes and have undergone thorough characterization (Hemelaar et al., 2017; Ong et al., 2018).

## 2.2 Experimental animals

Adult male C57BL/6J mice, aged 12 and 80 weeks, were purchased from Charles River Europe. The animals were housed in a controlled environment with regulated temperature and humidity. They were maintained on a 12-hour light/dark cycle, with food and water provided *ad libitum*. The mice were acclimatized for one week prior to the experiments. Euthanasia was performed by exsanguination under isoflurane/O2 anesthesia, after which livers, hearts, spleens, and kidneys were collected and preserved in ice-cold University of Wisconsin (UW) organ preservation solution (DuPont Critical Care) until further processing. All experimental protocols complied with Dutch regulations and were approved by the Institutional Animal Care and Use Committee of the University of Groningen and the Central Committee on Animal Experiments (permit number AVD10500202215969).

The experiment comprised three subparts. The first subpart involved four 80-week-old naturally aged mice to observe free radical accumulation and oxidative stress due to aging and to investigate the antioxidant properties of OBE100 in this context. The second part included four 12-week-old mice as a positive control group for the fatty acid-induced model to evaluate the extract's effects in young, non-stressed models. The third part comprised three 12-week-old mice treated with fatty acids to simulate hepatic steatosis, examining OBE100's efficacy under these conditions.

## 2.3 Precision-Cut Organ Slices

### 2.3.1 Slicing

The sample preparation for all batches of C57BL/6 male mice followed a consistent protocol. Initially, FNDs were sonicated in an ultrasonic bath for 10 minutes. The preparation of Krebs-Henseleit buffer, William's E Glucose Gentamicin (WEGG) solution, and sonification solution (SONOP) adhered to the protocol outlined by De Graaf et al. (I. A. de Graaf et al., 2010). Gentamicin is toxic to the kidney (Balakumar et al., 2010); therefore, for this organ, it was replaced with 100 μL of ciprofloxacin. The SONOP solution was then dispensed into 1.5 mL Eppendorf safe-lock tubes containing a measuring spoon of glass beads and used for collecting

and cryopreserving samples for viability assays and triglyceride estimation. For the WEGG-FND solution, 900 µL of FNDs were mixed with 17.1 mL of WEGG medium, resulting in a concentration of 50 µg/mL of FNDs.

Liver tissue was punctured using a 5 mm diameter biopsy needle while being exposed to Krebs-Henseleit buffer throughout the process. The biopsy samples were then placed in the sample holder of the Alabama Research and Development Tissue Slicer. The kidney was sliced whole by placing it directly into the core of the sample holder. Since the hearts and spleens of mice are generally small (for instance, a typical mouse heart has a transverse dimension of approximately 4.15 mm (Gargiulo et al., 2012)), these organs were first embedded in agarose. An agarose solution with a concentration of 3% was prepared by dissolving 3 grams of agarose in 100 mL of Milli-Q water (MQ water). The spleen and heart were slightly punctured with a needle to hold them in place, positioned in the core of the sample holder of the slicer, and then 2-3 mL of the agarose solution was poured over them. They were left for 5 minutes to polymerize, after which the needle was removed. This method provided better support for the heart and spleen, enabling the production of slices with uniform thickness.

The parameters of the slicer were calibrated to produce liver slices weighing approximately 4-5 mg, corresponding to a thickness of 200-250 µm, as determined in previous experiments (Bartucci et al., 2020). These parameters were applied to slice other organs as well. After slicing, PCS of the liver, heart, spleen, and kidney were obtained.

### 2.3.2 Collagenase Pre-Treatment

The collagenase solution was prepared by dissolving 6 mg of collagenase type 1 (or collagenase type 2 for the spleen) in 6 mL of WEGG solution (or William's E medium with glucose and ciprofloxacin for the kidney), resulting in a concentration of 0.1%. PCS of the liver designated for nanodiamond-based quantum sensing, and half of those from the kidney, spleen, and heart intended for FACS, underwent collagenase treatment in wells containing 500 µL of collagenase type 1 or type 2 solution. This procedure aimed to enhance the penetration of FNDs into the tissue and improve their cellular uptake. After incubating on a heating pad for 5 minutes, the samples underwent three 5-minute washes with UW solution. For the spleen, phosphate-buffered saline (PBS) was utilized instead as previous research in our project indicated that UW solution might reduce its viability.

## 2.4 OBE100 Treatment

### 2.4.1 Naturally Aged Mice

Following collagenase treatment, PCLS from the 80-week-old mice were transferred to wells containing 500 µL of WEGG-FNDs solution. After 24 hours, 3.7 µL of the OBE100 extract (100 µg/mL) was added by replacing an equivalent volume of the medium, excluding the baseline and control measurements. The PCLS were incubated with OBE100 for 6, 24, and 48 hours in a shaking incubator before being extracted for nanodiamond-based quantum sensing.

### 2.4.2  Positive Control Mice

A concentrated OBE100 solution (25 mg/mL) was prepared by dissolving 25 mg of OBE100 powder in 1 mL of dimethyl sulfoxide (DMSO). To achieve an OBE100 concentration of 100 µM, in each well 2 µL of this concentrated solution was added to 498 µL of WEGG. PCLS from 12-week-old positive control mice were incubated with the OBE100-WEGG solution for 6, 24, and 48 hours, with a medium change and a new dose of OBE100 administered after the 24-hour incubation.

### 2.4.3  Fatty Acid-Induced Mice

The PCLS from the 12-week-old mice were initially incubated for 48 hours in low-glucose Dulbecco's Modified Eagle Medium (DMEM), containing 10% fetal bovine serum, 1% antibiotics (penicillin and streptomycin), 1% bovine serum albumin (BSA), and 0.5 mM fatty acid mixture (sodium oleate and palmitate in a 2:1 ratio, i.e., 0.333 mM and 0.167 mM, respectively). Following a similar procedure to the positive control mice, the PCLS were incubated with OBE100-WEGG for 6, 24, and 48 hours, with a medium change after the 24-hour incubation.

## 2.5  Viability: ATP and Protein Assays

For viability assays, initial samples were collected from PCLS immediately after slicing. For the naturally aged mice, three tissue samples were placed in WEGG-FND solution as a 0-hour control before incubation with OBE100. For the fatty acid-induced mice, three samples were placed in WEGG medium as a 0-hour and fatty acid treatment control. Additionally, three samples were continuously incubated in WEGG medium for 48 hours to check for any viability changes in the PCLS without fatty acid treatment. Moreover, for this animal model, three samples were placed in WEGG-FND solution after fatty acid treatment. Additional viability samples were collected after incubation with OBE100 for 6, 24, and 48 hours, and after each T1 measurement. To evaluate the effects of OBE100 concentration, collagenase pre-treatment, and FNDs, PCLS after slicing underwent the preparation detailed in Section 2.5.1.

The viability assays were conducted to evaluate the impact of the OBE100 extract on tissue health and functionality and to validate the experimental conditions. The adenosine triphosphate (ATP)/protein ratio served as the primary outcome measure. Tissue viability depends on maintaining adequate ATP levels, with reductions in ATP indicating compromised viability (Bajerski et al., 2018). To standardize the measurements, ATP levels were normalized to protein content. The ATP assay for PCLS followed the method outlined by De Graaf et al. (I. A. de Graaf et al., 2010). After centrifugation, Eppendorf tubes containing the precipitate from the ATP assay were dried at 37 °C in an incubator for one day to prepare them for protein measurement. The protein assay was performed according to the manufacturer's instructions (Bio-Rad RC DC Protein Assay Kit I).

### 2.5.1  OBE100 Concentration

A concentrated OBE100 solution (25 mg/mL) was prepared by dissolving 25 mg of OBE100 powder into 1 mL of DMSO. From the concentrated OBE100 solution, subsequent dilutions

were prepared in each well of a 96-well plate: 2 µL of the concentrated solution was added to 498 µL of WEGG medium to achieve an OBE100 concentration of 100 µM, 1 µL was added to 499 µL of WEGG medium for a concentration of 50 µM, and 0.5 µL was added to 499.5 µL of WEGG medium to obtain 25 µM.

The control without collagenase was incubated in WEGG medium for 24 hours, while the control with collagenase underwent pre-treatment with collagenase (Section 2.3.2) before being incubated in WEGG medium for 24 hours.

Following pre-treatment with collagenase, PCLS were either first incubated for 24 hours with FNDs before the medium was exchanged to a WEGG solution with varying OBE100 concentrations, or they were immediately incubated with OBE100-WEGG without prior FND incubation. After 24 hours, a new dose of OBE100 was added by exchanging the medium with a fresh OBE100-WEGG solution.

## 2.6   Triglyceride Accumulation

The process commenced on the slicing day, with half of the collected PCLS undergoing collagenase pre-treatment (Section 2.3.2) to assess its impact on the cellular uptake of FNDs. Following this, PCLS were prepared using the same procedure as those for fatty acid-induced mice (Section 2.4.3). This included a 24-hour incubation with FNDs, followed by a 48-hour incubation in DMEM low-glucose medium containing a fatty acid mixture (i.e., fatty acid treatment). Subsequently, the PCLS were incubated with OBE100 (100 µg/mL) in OBE100-WEGG medium for 6, 24, and 48 hours. During the 48-hour incubation, the medium was changed after the initial 24 hours, administering a new dose of OBE100. Subsequently, three slices from each experimental condition (i.e., before any treatment, after fatty acid treatment with and without collagenase pre-treatment, and after incubation with OBE100 for 6, 24, and 48 hours with or without collagenase) were collected in separate Eppendorf safe-lock tubes and cryopreserved for fat analysis.

Fat isolation began by diluting a 10X TRIS-buffered saline (TBS) solution with MQ water to make 1X TBS. 600 µL of 1X TBS was added to each Eppendorf tube with samples and processed with a Minibead Beater 24 for 45 seconds. The samples were kept on ice for 5 minutes while preparing a set of 1.5 mL glass tubes. After 5 minutes, the samples were bead-beaten again for 45 seconds. Then, we collected 100 µL of the homogenate in new 1.5 mL Eppendorf tubes for later determination of protein content, which we used to normalize the triglyceride levels. The remaining homogenates were stored at $-80\,°C$. Subsequently, 300 µL of MQ water was added to the homogenate in the glass tubes and vortexed. 1500 µL of chloroform (2:1) was added to each glass vial in a fume hood. The samples were vortexed and stored on ice for 5 minutes, repeating this routine six times for each sample. 600 µL of MQ water was added to the homogenate in the glass tubes and vortexed. In the hood, 500 µL of chloroform was added to each glass tube and vortexed again. Afterward, the samples were centrifuged at 1500g for 10 minutes while a new set of glass tubes was prepared. Following centrifugation, the bottom layer (chloroform containing fat) was collected into the new glass tubes and air-dried in the hood overnight for triglyceride estimation.

In the fume hood, the dried isolated fat samples were reconstituted by adding 600 µL of 2% Triton X-100% chloroform. After thorough vortexing, they were air-dried overnight on a heating pad. From here, triglyceride estimation was carried out using the Trig/GB kit (Roche Molecular

Biochemicals), following the manufacturer's instructions.

Protein estimation after fat isolation began by adding 100 µL of 5M sodium hydroxide (NaOH) to the air-dried homogenates, followed by incubation for 30 minutes at 37 °C in the water bath under high-speed and shaking conditions. Concurrently, a thawed aliquot of BSA (3.2 mg/mL) was used to prepare a calibration curve: 50 µL of BSA was mixed with 50 µL of 1M NaOH to achieve a concentration of 1.6 µM. From this solution, 0.8, 0.4, 0.2, and 0.1 µM and 0.0 µM BSA solutions in NaOH were prepared. After incubation, 400 µL of MQ water was added to each sample tube and homogenized using the minibead-beater for 40 seconds. Then, 5 µL of each sample and calibration curve were pipetted in duplicate into designated wells of a transparent 96-well plate. Subsequently, 25 µL of reagent A was added to each well, followed by 200 µL of reagent B. The plate was incubated for 15 minutes at room temperature in the dark. Then, we measured the absorbance at 650 nm using the standard settings of the Synergy Lowry Assay protocol on a Synergy HT plate reader.

## 2.7 Free Radical Measurements with Nanodiamond-Based Quantum Sensing

The nanodiamond magnetometer used in this study was developed in-house. It functioned as a confocal microscope, featuring sensitive detection capabilities with an avalanche photodiode and pulsing. The laser used had a wavelength of 561 nm, and the equipment had a numerical aperture of 0.75. The experimental setup for the nanodiamond magnetometer was similar to that of described by Morita et al. (2020), with a notable modification involving the addition of an incubator and the use of a different wavelength laser (the original setup utilized a laser with a wavelength of 532 nm).

Prior to each T1 measurement, PCLS were placed in Petri dishes containing 2 mL of WEGG solution and secured with an anchor. Nanodiamond particles were identified based on their fluorescence through visual inspection of images. Criteria for stable nanodiamond identification included a fluorescence signal exceeding 600 counts per second, consistent photon counting with minimal fluctuations and values at or above one million, and minimal movement of the diamond when centered in view. The tracking algorithm described by Li et al. (R. Li et al., 2022) was then initiated to begin nanodiamond-based quantum sensing measurements.

In total 43 dark times were used, and the pulse sequence was repeated 10 000 times for each T1 measurement to reduce noise. To enhance clarity, background light in the images was eliminated by applying a filter to exclude pixels with values less than 80. The process was replicated at least three times for each experimental condition: time points at 6, 24, and 48 hours, as well as baseline measurements at 24 and 48 hours. For fatty acid-induced mice, additional measurements were taken after fatty acid treatment, and following prolonged incubation of 24 and 48 hours in the WEGG medium.

In this experiment, NV center ensembles hosted in nanodiamonds were utilized. The decision was based on the enhanced brightness of NV center ensembles, enabling easier detection even amidst background fluorescence. Moreover, employing ensembles inherently reduces variability between particles (Perona Martinez et al., 2020).

## 2.8 Statistical Analysis

### 2.8.1 Nanodiamond-Based Quantum Sensing

The data fitting model for spin ensembles was adopted from Perona Martinez et al. (2020).

Two outlier analyses were performed. Initially, values below 50 and above 800 were manually excluded, as they were not physically plausible for our nanodiamonds or could result from detection limitations. Subsequently, the Robust Regression and Outlier Removal method in GraphPad Prism was applied, with a False Discovery Rate set at 1%. A one-way ANOVA test with a 95% CI was used to determine if the means of distinct experimental conditions differed significantly. To pinpoint specific statistically significant differences among these conditions, Tukey's multiple comparison test, a pairwise post hoc test, was applied. Graphs were generated using cleaned data post-outlier analysis, incorporating results from Tukey's test.

### 2.8.2 Viability Assays and Triglyceride Estimation

The data analysis for viability assays and triglyceride estimation involved similar procedures, utilizing the measured standard curves for each analyte.

For ATP estimation in pmol, a logarithmic transformation was applied. Initially, average values of ATP content (A) and their logarithms ($\log A$) were computed for each experimental condition. Subsequently, Formula 1 was employed using the respective standard curve, where Y denoted the y-intercept of the calibration curve and k was its slope:

$$10^{\frac{\log A - Y}{k}} \cdot 10 \tag{1}$$

The resulting figure represented a 10-fold dilution, which was subsequently multiplied by $10^9$ to determine ATP per PCLS.

To ascertain the concentration of triglycerides in µg/mL and protein concentration in mg/mL, we utilized Formula 2 based on the standard curve.

$$\frac{A - Y}{k} \tag{2}$$

Subsequently, we computed the ATP/protein and triglyceride/protein ratios, followed by determining the mean and standard deviation for each experimental condition. The statistical analysis followed procedures akin to those employed in nanodiamond-based quantum sensing (Section 2.8.1). To determine if the means of two groups differed statistically, an unpaired t-test with Welch's correction and a 95% CI was applied.

## 2.9 FACS

FACS was conducted prior to my involvement in the project. The procedure began with tissue dissociation, wherein PCS of the heart, kidney, and spleen were collected in separate Eppendorf tubes, each containing 1 ml PBS. For the kidney and heart, five PCS were collected in one tube as a sample, whereas for the spleen, fifteen PCS were collected per tube due to the smaller size

of spleen PCS. Subsequently, PCS of each organ, along with PBS, were transferred to a 100 µm cell strainer (EASYstainer from Greiner Bio-One) placed on a Petri dish and mechanically meshed. Following each sample, the mortar was rinsed with 70% ethanol and MQ water, and dried with a paper towel. The tubes were centrifuged at 300 x g at 4 °C for 10 minutes, after which the supernatant was removed.

The subsequent procedure involved blocking Fc receptors to inhibit the non-specific binding of fluorescently labeled antibodies. This was achieved using TruStain FcX (anti-CD16/CD32) at a concentration of 1 µg per $10^6$ cells in 100 µL, along with 9.5 µL of TruStain and 490.5 µL of PBS per sample. The samples were then incubated for 15 minutes at 4 °C and centrifuged at 300 x g at 4 °C for 5 minutes.

Staining was performed by resuspending the samples in 200 µL of PBS containing appropriate stains. Each spleen sample was treated with 2 µL of CD68 (PE-Vio 770, Miltenyi Biotec) for macrophages, 2.5 µL of CD3ε (VioBlue, Miltenyi Biotec) for T cells, and 1.25 L of CD19 (AF647, BioLegend) for B cells.

For kidney samples, 2.5 µL of CD68 (PE-Vio 770), 2.5 µL of CD34 (APC-Fire 750, BioLegend) for endothelial cells, 2.5 µL of CD140a (BV605, BioLegend) for fibroblasts, and 2.5 µL of podoplanin (BV421, BioLegend) for podocytes were used. Additionally, 50 µL of Brilliant Stain Buffer was added to restore expected fluorescent staining patterns, as BD Horizon Brilliant reagents were used.

Each heart sample was treated with 2 µL of CD68 (PE-Vio 770) for macrophages, 2.5 µL of CD34 (APC-Fire 750) for endothelial cells, 2.5 µL of CD140a (BV605) for fibroblasts, 1 µL of NG2 (FITC, Biorbyt) for pericytes, and 50 µL of Brilliant Stain Buffer.

The samples were then incubated for 30 minutes at room temperature in the dark. Following this, they were centrifuged at 300 x g at 4 °C for 5 minutes, and the supernatant was carefully removed. The tubes were subsequently washed with 1 mL of PBS. Another centrifugation step was performed at 300 x g at 4 °C for 5 minutes, and once again, the supernatant was carefully removed.

For fixation, 500 µL of 4% paraformaldehyde was added, and the samples were incubated for 15 minutes at room temperature in the dark. Subsequently, they were centrifuged at 300 x g at 4 °C for 5 minutes, and the supernatant was removed. The samples underwent washing with 1 mL of PBS, followed by centrifugation at 300 x g at 4 °C for 5 minutes, and removal of the supernatant. This washing step was repeated twice. Finally, the samples were resuspended in 1 mL of PBS for flow cytometry analysis. After FACS, cells were permeabilized with PBS-T (0.1%) for 10 minutes at room temperature in the dark. They were then incubated with PBS-T containing DAPI (1:100) and Oregon Green 488 Phalloidin (1:40) for 20 minutes at room temperature in the dark. Following incubation, the cells were washed once with PBS-T, and the slides were mounted with ProLong Diamond Antifade Mountant.

## 2.10   Image Acquisition and Analysis

The slides prepared for analysis underwent examination using confocal microscopy. XYZ images were captured using the LeicaSP8X laser scanning confocal microscope equipped with an HC PL APO OIL C52 objective (63x, N.A.1.40) and 405, 495, and 561 nm laser lines, according to the Nyquist criterion. For the objective, Immersion Oil Type FF (purchased from Electron

Microscopy Sciences) was used. Cell identification was facilitated by DAPI staining for nuclei and FITC-phalloidin staining for actin filaments (Figure 4, b, c). The red/near-infrared fluorescence (630-800 nm) emitted by FNDs when excited with green laser light, attributed to the NV defect, facilitated their recognition (Schirhagl et al., 2014). After cell identification, the lower and upper z positions were determined, and Z-stacks of 2D images with a step size of 0.2 μm were generated. The Z-stack was then visually inspected to detect the presence of FNDs within the cell. The FNDs appeared as small, bright red dots or larger irregularly shaped dots in the case of FND clusters, significantly brighter than the background (Figure 4, d). A total of 100 cells were analyzed per imaged sample, or as many cells as possible if the full count was not feasible.
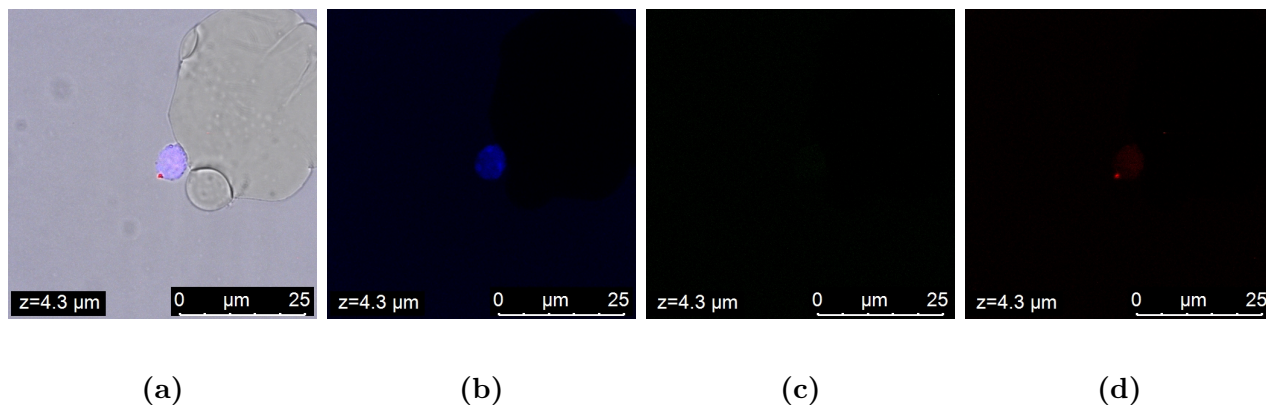


**(a)** **(b)** **(c)** **(d)**

**Figure 4.** Example of a confocal image with various channels. (a) Overlap of all staining channels with the brightfield channel. (b) Channel visualizing DAPI staining of nuclei in blue. (c) Channel visualizing FITC-phalloidin staining for actin filaments in green. (d) Channel visualizing FNDs in red; a cluster of FNDs is seen as a bright red dot.

# 3   Results

## 3.1   Nanodiamond Based Quantum Sensing

### 3.1.1   OBE100 Effect on Free Radicals in Naturally Aged Mice

Turkey's multiple comparison test with a 95% CI reveals no statistically significant differences between the two baseline measurements: one with a 24-hour incubation with FNDs in WEGG medium and the other with a 48-hour incubation. A trend of increasing T1 values is observed up until the incubation with OBE100 for 24 hours, which shows statistically significant differences compared to both the 24-hour baseline measurement (control[1]) and the 48-hour baseline measurement. A decrease in T1 values, although not statistically significant, is observed with a 48-hour continuous incubation with OBE100 (Figure 5).

---

[1]The 24-hour baseline serves as a control, as all PCLS underwent a preliminary 24-hour incubation with FNDs before exposure to OBE100
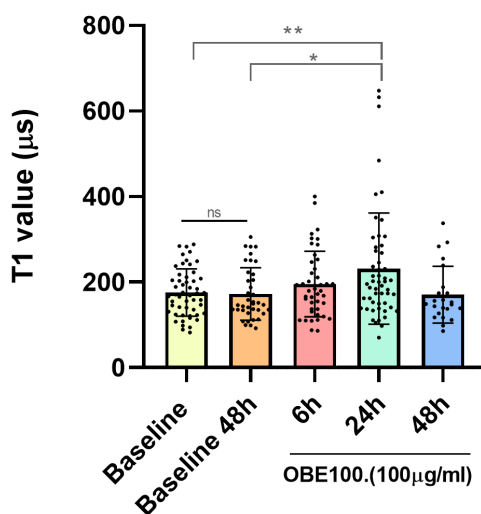
**Figure 5.** T1 values reflecting free radical accumulation in PCLS from all naturally aged mice before and after incubation with OBE100. Each data point represents an individual T1 measurement, with bars indicating mean values and error bars representing standard deviations. Higher T1 values indicate reduced free radical accumulation around the FND probe. A statistically significant increase in T1 values is observed after 24 hours of incubation compared to both baselines, followed by a non-significant decrease at 48 hours.

### 3.1.2 OBE100 Effect on Free Radicals in Positive Control Mice

Turkey's multiple comparison test with a 95% CI displays no statistically significant differences among the baseline measurements (24 and 48-hour incubation with FNDs in WEGG) themselves, nor between these baselines and the continuous incubation with OBE100 for 6, 24, and 48 hours. However, a highly statistically significant increase in T1 values is observed between both baseline measurements and the 48-hour incubation with OBE100, when a medium change and a new dose of the extract were administered after the first 24 hours (Figure 6).

### 3.1.3 OBE100 Effect on Free Radicals in Fatty Acid-Induced Mice

Turkey's multiple comparison test with a 95% CI demonstrates a highly statistically significant difference between the baseline measurement after 24-hour incubation with FNDs in WEGG medium and the measurement after an additional 48-hour fatty acid treatment. No statistically significant differences are observed after the fatty acid treatment when the tissue has been incubated for 24 and 48 hours in WEGG medium. A highly statistically significant difference in T1 values is observed with a 48-hour incubation with OBE100, with a medium change and a new dose of the extract administered after the first 24-hour incubation. Notably, this value shows no statistically significant difference from the baseline measurement. An increase, though not statistically significant, is observed between the T1 values after the fatty acid treatment

**Effect of OBE100 on Free radicals in PCLS of PC mice**
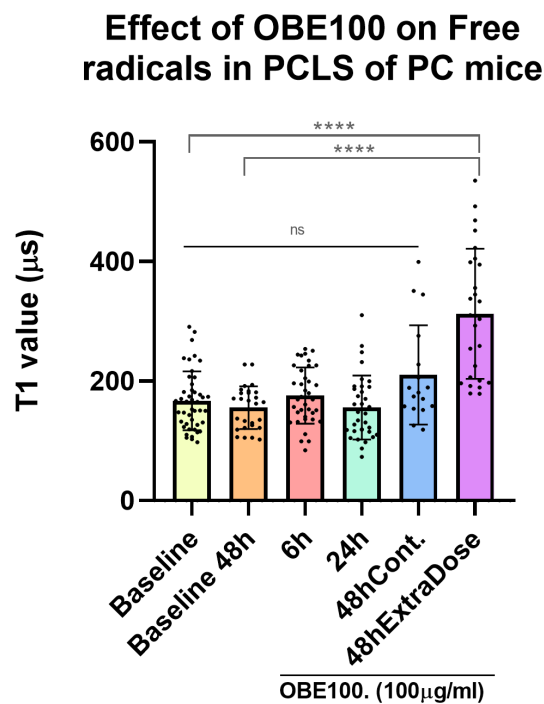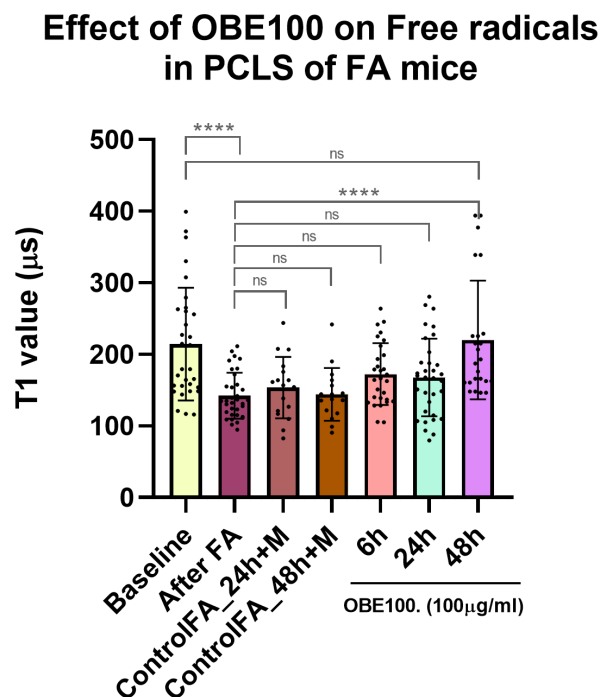
n= 4; C57bL/6 male mouse; p<0.05; post hoc test

**Figure 6.** T1 values reflecting free radical accumulation in PCLS from all positive control mice before and after incubation with OBE100. Each data point represents an individual T1 measurement, with bars indicating mean values and error bars representing standard deviations. Higher T1 values indicate reduced free radical accumulation around the FND probe. No statistically significant differences are observed between baseline measurements and continuous incubation with OBE100. However, a highly statistically significant rise in T1 values occurs after 48 hours of incubation with OBE100, following an additional dose and medium change after the initial 24 hours.

and the incubation with OBE100 for 6 and 24 hours (Figure 7).

## 3.2 Triglyceride Accumulation

Following the fatty acid treatment of PCLS, Tukey's multiple comparison test with a 95% CI reveals a highly statistically significant increase in triglyceride levels, regardless of whether the PCLS underwent collagenase pre-treatment. For samples treated with collagenase, incubation with OBE100 for 6 and 24 hours does not indicate any statistically significant differences compared to the triglyceride/protein values post-fatty acid treatment, with a statistically significant decline appearing only after 48-hour incubation. In contrast, for samples without collagenase, a statistically significant reduction in triglyceride levels is observed as early as 6 and 24 hours of incubation with OBE100, which becomes highly statistically significant after 48 hours (Figure 8).

An unpaired t-test with Welch's correction at 95% CI reveals no statistically significant difference between the mean triglyceride/protein values after fatty acid treatment with and without

**Effect of OBE100 on Free radicals in PCLS of FA mice**

n= 3; C57bL/6 male mouse; p<0.05; post hoc test

**Figure 7.** T1 values reflecting free radical accumulation in PCLS from all fatty acid-induced mice before and after incubation with OBE100. Each data point represents an individual T1 measurement, with bars indicating mean values and error bars representing standard deviations. Higher T1 values indicate reduced free radical accumulation around the FND probe. A highly statistically significant increase in T1 values is observed after a 48-hour incubation with OBE100, which included a medium change and an additional dose following the initial 24 hours. The 48-hour incubation shows no statistically significant difference from the baseline measurement.

collagenase pre-treatment (Figure 9).

## 3.3 Viability Assessment

### 3.3.1 OBE100 Concentration, Incubation With FNDs, Collagenase Pre-treatment

One-way ANOVA with a 95% CI reveals no statistically significant differences among the means of distinct experimental conditions (i.e., $p > 0.05$). However, the ATP and protein assays indicate a trend of decreasing ATP/Protein ratio values with increasing OBE100 concentration, suggesting compromised viability. This trend is observed for both PCLS incubated with or without FNDs (Figure 10, c and d). The collagenase treatment is associated with decreased ATP/Protein ratio values (Figure 10, b), and there is no discernible impact of FND incubation on viability (Figure 10, a).
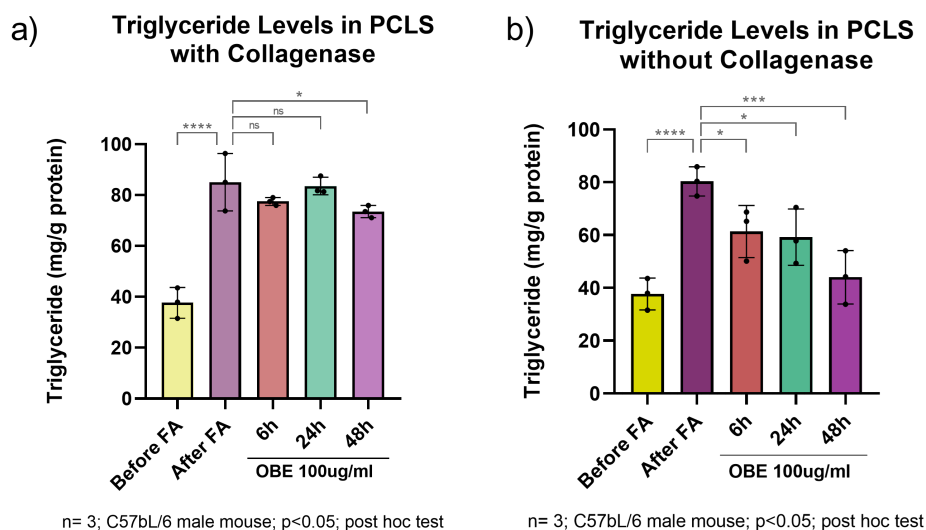
**Figure 8.** Assessment of triglyceride levels in PCLS following OBE100 treatment, with comparison to pre- and post-fatty acid treatment values. Each data point represents an individual PCLS sample, with bars indicating mean triglyceride value and error bars showing standard deviations. (a) Triglyceride estimation with collagenase treatment, revealing a statistically significant decrease after 48-hour incubation with OBE100. (b) Triglyceride assessment without collagenase treatment, demonstrating a statistically significant decline after 6 and 24 hours of incubation with OBE100, with further reduction becoming highly statistically significant after 48 hours.
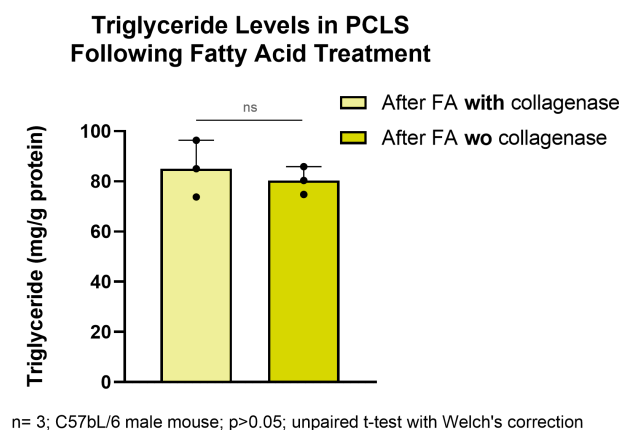


**Figure 9.** Comparison of triglyceride levels following fatty acid treatment with and without collagenase pre-treatment reveals no statistically significant differences. Each data point represents an individual PCLS sample, with bars indicating the mean triglyceride value and error bars representing standard deviations.

### 3.3.2  OBE100 Treatment in Naturally Aged Mice

According to the one-way ANOVA test with a 95% CI, no statistically significant differences are observed among the means of different experimental conditions for the PCLS obtained
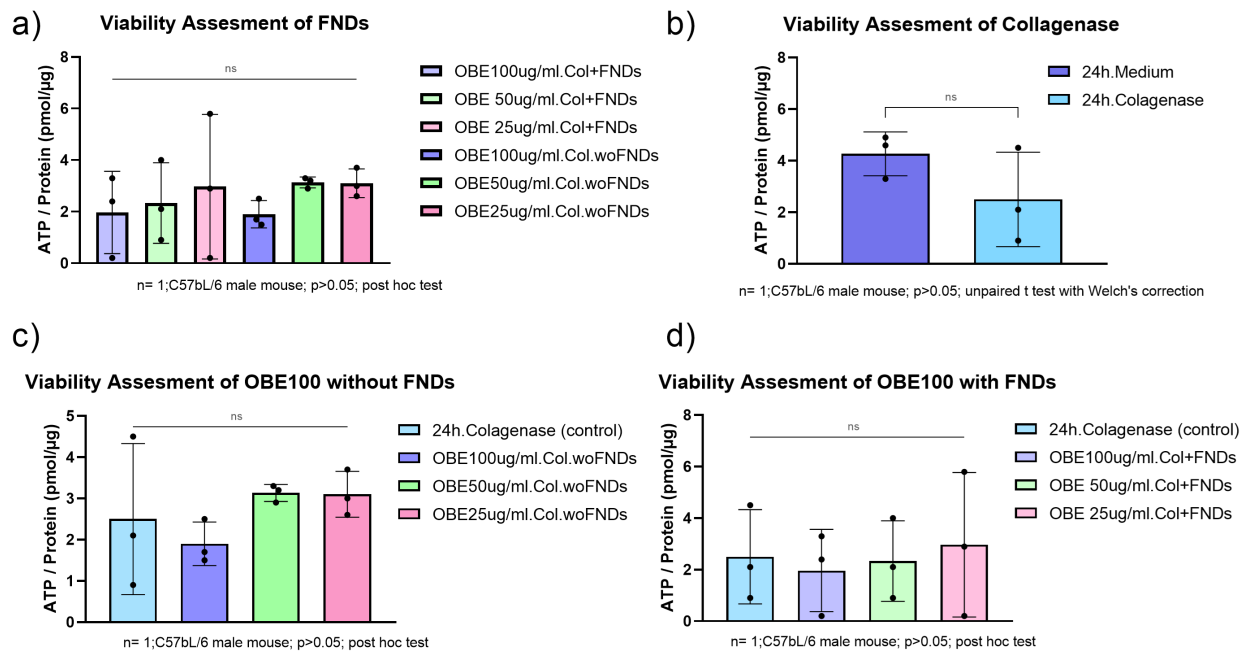
**Figure 10.** Viability assessment of PCLS treated with collagenase, FNDs, and various concentrations of OBE100. Each data point represents an individual PCLS sample, with bars indicating mean ATP/protein ratio (a measure of cellular viability) and error bars showing standard deviations. (a) Comparison of ATP/Protein ratio values for different OBE100 concentrations, with or without FNDs, shows no statistically significant differences. (b) Assessment of collagenase treatment reveals a non-significant decreasing trend in viability. (c) and (d) Evaluation of OBE100 concentration on PCLS viability, with or without FNDs, demonstrates a declining trend with increasing OBE100 concentration, but without statistical significance in both cases.

from naturally-aged mice (i.e., $p > 0.05$). This encompasses comparisons between the 24-hour incubation with FNDs and the incubation with both FNDs and OBE100 for 6, 24, and 48 hours, the comparison of the baseline T1 measurement and incubation with OBE100 for various durations following incubation with FNDs and post-T1, and the evaluation of viability before and after T1 measurements. A trend of decreasing ATP/Protein values is observed as the incubation with OBE100 progresses and when comparing the PCLS following this incubation with those after T1 measurements (Figure 11, a, c).

### 3.3.3 OBE100 Treatment in Positive Control Mice

One-way ANOVA with a 95% CI reveals no significant statistical differences among various incubation times with OBE100 and FNDs and the 24-hour incubation with FNDs. A trend of declining ATP/Protein ratio values is observed for incubation with OBE100 over increasing durations; however, these changes are not statistically significant (Figure 12, a).

No statistically significant differences are detected between the 24-hour baseline and the PCLS incubated with OBE100 and FNDs for various durations following T1 measurements (Figure 12, b).
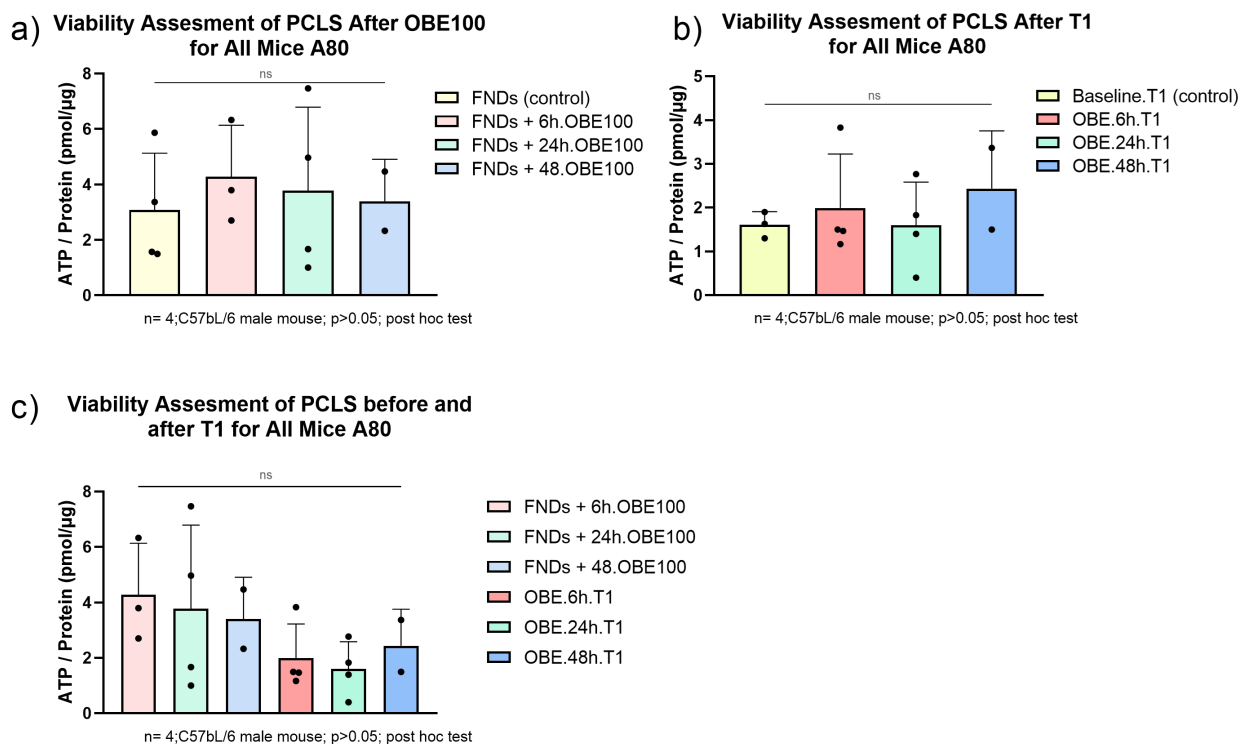
**Figure 11.** Viability assessment of PCLS from naturally-aged mice. Each data point represents the average ATP/Protein ratio per animal model under different experimental conditions. Bars indicate mean ATP/Protein ratios, with error bars showing standard deviations. (a) Effect of OBE100 treatment on PCLS viability following pre-incubation with FNDs, compared to FNDs alone as a control, shows no statistically significant differences across incubation times. (b) Evaluation of T1 measurements on PCLS viability reveals no statistically significant differences between the 24-hour baseline (control with FNDs and medium) and various OBE100 incubation durations. (c) Comparison before and after T1 measurements indicates no statistically significant changes in viability.

Comparing viability before and after T1 measurements, a statistically significant decrease is observed between both the 6-hour and 24-hour incubations with OBE100 and FNDs and all incubations with OBE100 at varying time intervals after T1 (Figure 12, c).

### 3.3.4 OBE100 Treatment in Fatty Acid-Induced Mice

One-way ANOVA with a 95% CI shows no statistically significant differences between the means of the various experimental conditions. An increase in ATP/Protein ratio values is noted between PCLS without incubation with FNDs and the fatty acid treatment (day of slicing), and those with 0-hour incubation with FNDs before the fatty acid treatment (one day after slicing). A similar increase is also detected after 48 hours without treatment (Figure 13, a).

No statistically significant differences are noted between the 24-hour baseline and the PCLS samples incubated with OBE100 and FNDs for varying durations after T1 measurements (Fig-

**Figure 12.** Viability assessment of PCLS from positive control mice. Each data point represents the average ATP/Protein ratio per animal model under different experimental conditions. Bars indicate mean ATP/Protein ratios, with error bars showing standard deviations. (a) Effect of OBE100 treatment on PCLS viability following pre-incubation with FNDs, compared to FNDs alone, shows no significant differences across incubation times. A trend of declining ATP/Protein ratio values is noted with increasing OBE100 incubation durations. (b) The assessment of T1 measurements on PCLS viability reveals no statistically significant differences between the 24-hour baseline and OBE100-treated PCLS at various post-T1 incubation times. (c) Viability comparison before and after T1 measurements indicates a significant decrease between 6-hour and 24-hour incubations with OBE100 and FNDs and all OBE100 incubation intervals post-T1 measurements.

ure 13, b).

Additionally, a decrease in viability is observed after fatty acid treatment, and as the incubation with OBE100 progresses; however, neither is statistically significant (Figure 13, a).

Furthermore, a reduction in ATP/Protein ratio is detected between PCLS incubated with OBE100 and FNDs at varying time intervals and those that underwent T1 measurements after the same incubation (Figure 13, c).
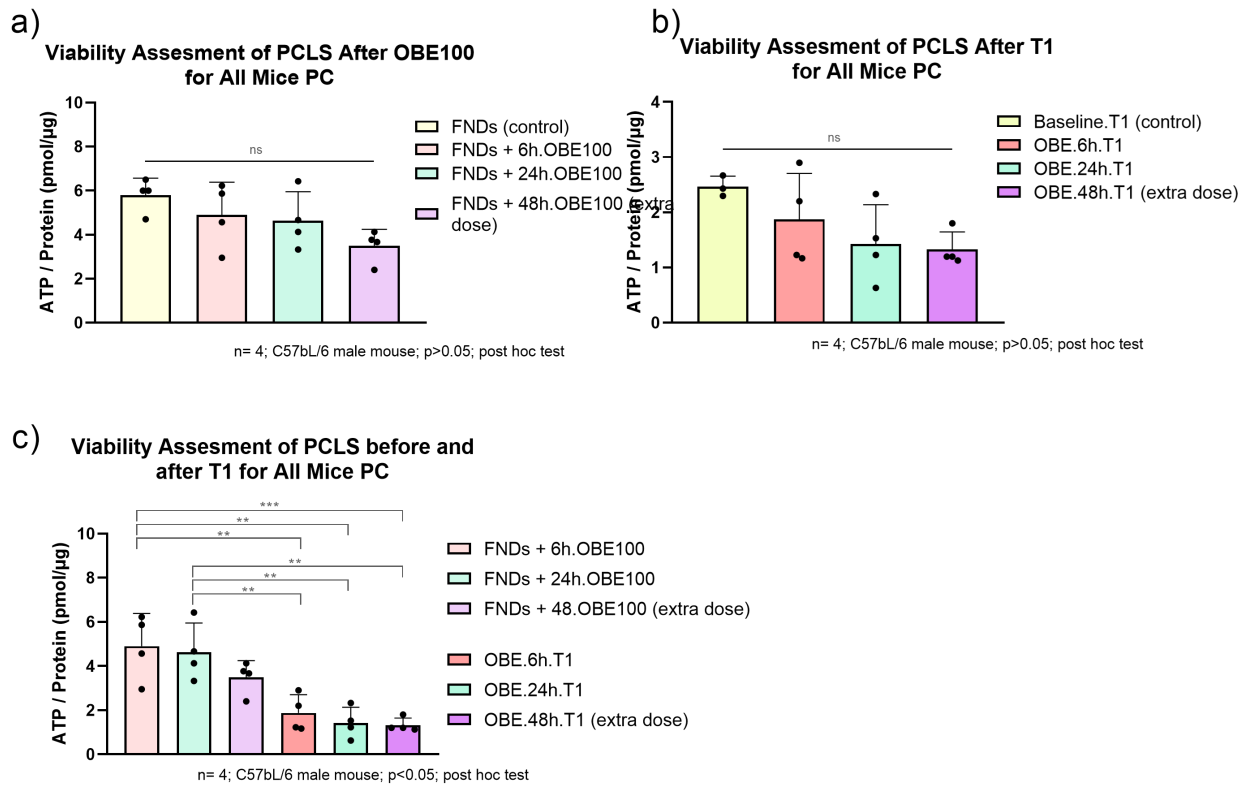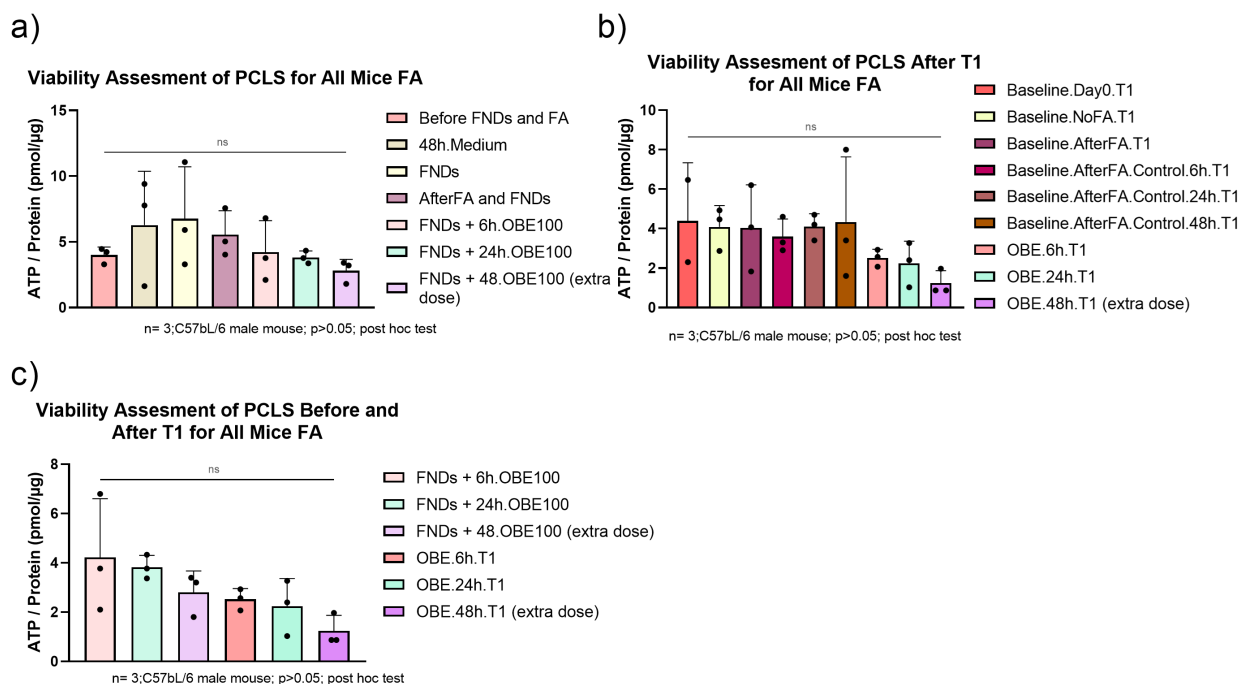
27

**Figure 13.** Viability assessment of PCLS from fatty acid-induced mice. Each data point represents the average ATP/Protein ratio per animal model under different experimental conditions. Bars indicate mean ATP/Protein ratios, with error bars showing standard deviations. (a) Effects of treatments including FNDs, fatty acid exposure, and OBE100 incubation on PCLS viability, revealing no statistically significant differences. Decreasing viability trends are observed from PCLS incubated with FNDs before versus after fatty acid treatment and with prolonged OBE100 incubation. Conversely, an increase in viability is noted from PCLS before any treatment to after 24-hour FND incubation and 48-hour medium incubation. (b) Effect of T1 measurements on PCLS viability across experimental conditions, showing no statistically significant differences. (c) Viability comparison before and after T1 measurements indicates no statistically significant differences, however, it reveals a trend of reduced viability post-T1 measurements.

## 3.4 Distribution of Fluorescent Nanodiamonds

### 3.4.1 Splenic Cells

Macrophages (CD68+) demonstrate the highest FND uptake in splenic cells, particularly without collagenase pre-treatment (59% of cells imaged with confocal microscopy contain at least one FND, compared to 28% with collagenase pre-treatment) (Figure 14). However, it is important to note that obtaining a full count of 100 cells has not been feasible in any of the samples of splenic macrophages; in one, only four cells were counted (Table 1).

B cells show increased internalization of FNDs following collagenase treatment, yet this uptake remains significantly lower than that observed in macrophages, especially those without collagenase treatment. The 'all-negative' category, encompassing cells negative for any sorting markers used, demonstrates similar uptake levels, though collagenase diminishes it in this group. In one of the three 'all-negative' samples, a full cell count was unfeasible, with only

18 cells counted (Table 1). T cells exhibit the lowest FND uptake, which is enhanced with collagenase pre-treatment (Figure 14).
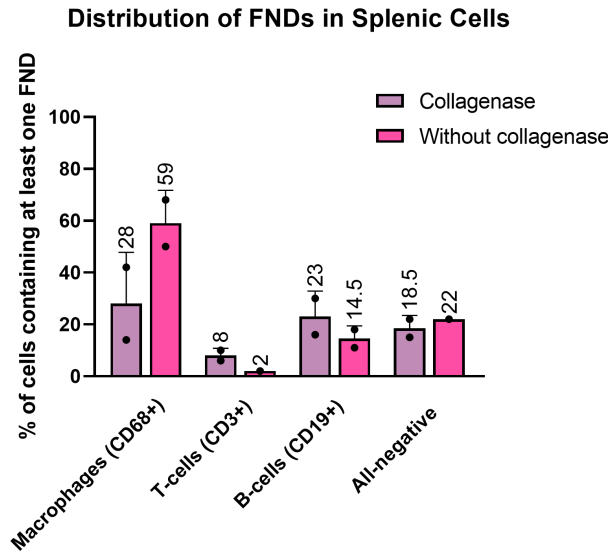


**Figure 14.** Distribution of FNDs among FACS-sorted cells from the spleen. Each data point represents the percentage of cells containing at least one FND. Data from two animals is included. Bars indicate the mean percentage (displayed above each bar), and error bars represent the standard deviation. For macrophages and "all-negative" cells, FND uptake decreases with collagenase pre-treatment, while the opposite is true for T and B cells. The majority of FNDs are uptaken by macrophages, particularly in samples not treated with collagenase.

Table 1: Distribution of FNDs among different FACS-sorted splenic cell types. The table presents the total number of cells counted, the number of cells with FNDs, and the percentage of cells with FNDs for each cell type and "all-negative" category. Data are shown for samples with and without collagenase pre-treatment. Samples were taken from two animals, however, not all cell types were sorted in each sample.

| Cell Type | Collagenase Pre-Treatment | Total Cells Counted | Cells with Diamonds | % Cells with Diamonds |
|-----------|---------------------------|---------------------|---------------------|------------------------|
| Macrophages (CD68+) | Yes | 71* | 30 | 42 |
| | | 44* | 6 | 14 |
| | No | 4* | 2 | 50 |
| | | 50* | 34 | 68 |
| T-cells (CD3+) | Yes | 100 | 6 | 6 |
| | | 100 | 10 | 10 |
| | No | 100 | 2 | 2 |
| B-cells (CD19+) | Yes | 100 | 16 | 16 |
| | | 100 | 30 | 30 |

Table 1: Distribution of FNDs among different FACS-sorted splenic cell types. The table presents the total number of cells counted, the number of cells with FNDs, and the percentage of cells with FNDs for each cell type and "all-negative" category. Data are shown for samples with and without collagenase pre-treatment. Samples were taken from two animals, however, not all cell types were sorted in each sample. (Continued)

| Cell Type | Collagenase Pre-Treatment | Total Cells Counted | Cells with Diamonds | % Cells with Diamonds |
|---|---|---|---|---|
| *All-negative* | No | 100 | 11 | 11 |
| | | 100 | 18 | 18 |
| | Yes | 100 | 15 | 15 |
| | | 18* | 4 | 22 |
| | No | 100 | 22 | 22 |

\* Instances where the full cell count of 100 cells was not attainable

### 3.4.2 Kidney Cells

Kidney cells, like splenic cells, exhibit the highest FND uptake in macrophages (CD68+) without collagenase pre-treatment, with 58% of imaged cells containing at least one FND. In macrophages, full counts were unfeasible in one collagenase-treated sample and one untreated sample, with 38 and 41 cells counted, respectively. The "all-negative" category without collagenase also shows high uptake, though full counts were attainable in only half of these samples. Both macrophages and "all-negative" cells demonstrate higher FND internalization without collagenase. Endothelial cells (CD34+) show relatively high FND uptake, which is enhanced by collagenase treatment. Only one sample did not reach the full number of cells, but it still obtained a near-full count with 93 cells. Podocytes (Podoplanin+) exhibit high FND uptake regardless of pre-treatment (Figure 15), with two samples (one with and one without collagenase) where full counts were unattainable, counting only 11 and 5 cells respectively (Table 2).

Table 2: Distribution of FNDs among different FACS-sorted kidney cell types. The table presents the total number of cells counted, the number of cells with FNDs, and the percentage of cells with FNDs for each cell type and "all-negative" category. Data are shown for samples with and without collagenase pre-treatment. Samples were taken from three animals.

| Cell Type | Collagenase Pre-Treatment | Total Cells Counted | Cells with Diamonds | % Cells with Diamonds |
|---|---|---|---|---|
| *Macrophages (CD68+)* | Yes | 38* | 7 | 18 |
| | | 100 | 30 | 30 |
| | | 100 | 68 | 68 |
| | No | 41* | 18 | 44 |
| | | 100 | 56 | 56 |
| | | 100 | 74 | 74 |

**Figure 15.** Distribution of FNDs among FACS-sorted cells from the kidney. Each data point represents the percentage of cells containing at least one FND. Data from three animals is included. Bars indicate the mean percentage (displayed above each bar), and error bars represent the standard deviation. For macrophages and "all-negative" cells, FND uptake decreases with collagenase pre-treatment, while the opposite is true for endothelial cells and podocytes. The majority of FNDs are taken up by macrophages, especially in samples not treated with collagenase; however, other cell types also show similar levels of FND internalization.

Table 2: Distribution of FNDs among different FACS-sorted kidney cell types. The table presents the total number of cells counted, the number of cells with FNDs, and the percentage of cells with FNDs for each cell type and "all-negative" category. Data are shown for samples with and without collagenase pre-treatment. Samples were taken from three animals. (Continued)

| | | | | |
|---|---|---|---|---|
| | | 100 | 19 | 19 |
| | Yes | 100 | 47 | 47 |
| | | 100 | 66 | 66 |
| Endothelial cells (CD34+) | | 100 | 12 | 12 |
| | No | 100 | 46 | 46 |
| | | 93* | 30 | 32 |
| | | 11* | 3 | 27 |
| | Yes | 100 | 25 | 25 |
| | | 100 | 62 | 62 |
| Podocytes (Podoplanin+) | | 5* | 1 | 20 |
| | No | 100 | 33 | 33 |

31

Table 2: Distribution of FNDs among different FACS-sorted kidney cell types. The table presents the total number of cells counted, the number of cells with FNDs, and the percentage of cells with FNDs for each cell type and "all-negative" category. Data are shown for samples with and without collagenase pre-treatment. Samples were taken from three animals. (Continued)

| Cell Type | Collagenase Pre-Treatment | Total Cells Counted | Cells with Diamonds | % Cells with Diamonds |
|---|---|---|---|---|
| All-negative | | 100 | 56 | 56 |
| | | 18* | 2 | 11 |
| | Yes | 100 | 18 | 18 |
| | | 100 | 60 | 60 |
| | | 3* | 1 | 33 |
| | No | 100 | 35 | 35 |
| | | 76* | 59 | 78 |

* Instances where the full cell count of 100 cells was not attainable

### 3.4.3 Heart Cells

Compared to sorted cells from spleen and kidney, heart cells exhibit the lowest FND internalization levels. The highest uptake of FNDs is observed in the 'all-negative' category without collagenase pre-treatment (25.33%). However, for "all-negative" samples, the full cell count was attained in only one case, with the rest having cell numbers between 0 and 35. Pericytes (NG2+) show the next highest uptake, with the full count not achievable in only one case when 73 cells were counted. Fibroblasts (CD140a+/CD34+) exhibit the lowest FND uptake at 13% with collagenase treatment and 2.5% without. However, the full cell count was achieved in only one of the four samples; in the remaining cases, 3 or 6 cells were counted (Figure 16, Table 3).

Table 3: Distribution of FNDs among different FACS-sorted heart cell types. The table presents the total number of cells counted, the number of cells with FNDs, and the percentage of cells with FNDs for each cell type and "all-negative" category. Data are shown for samples with and without collagenase pre-treatment. Samples were taken from three animals, however, not all cell types were sorted in each sample.

| Cell Type | Collagenase Pre-Treatment | Total Cells Counted | Cells with Diamonds | % Cells with Diamonds |
|---|---|---|---|---|
| Pericytes (NG2+) | | 100 | 9 | 9 |
| | Yes | 73* | 3 | 4 |
| | | 100 | 57 | 57 |
| | | 100 | 11 | 11 |
| | No | 100 | 15 | 15 |
| | | 100 | 39 | 39 |
| Fibroblasts (CD140a+/CD34+) | Yes | 6* | 0 | 0 |

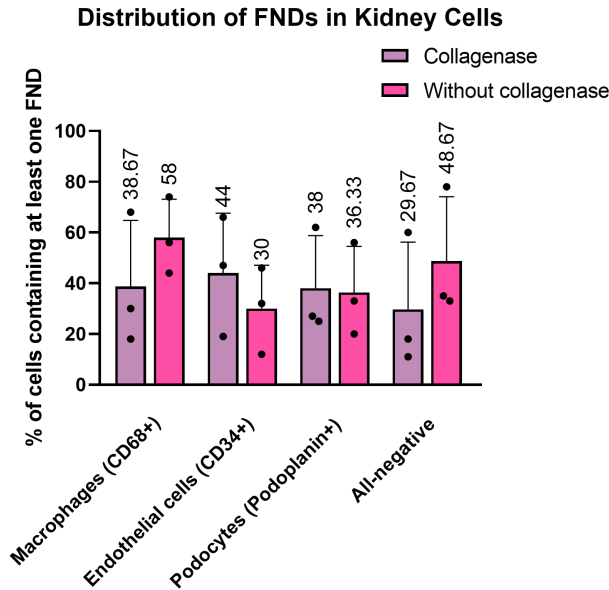**Distribution of FNDs in Heart Cells**
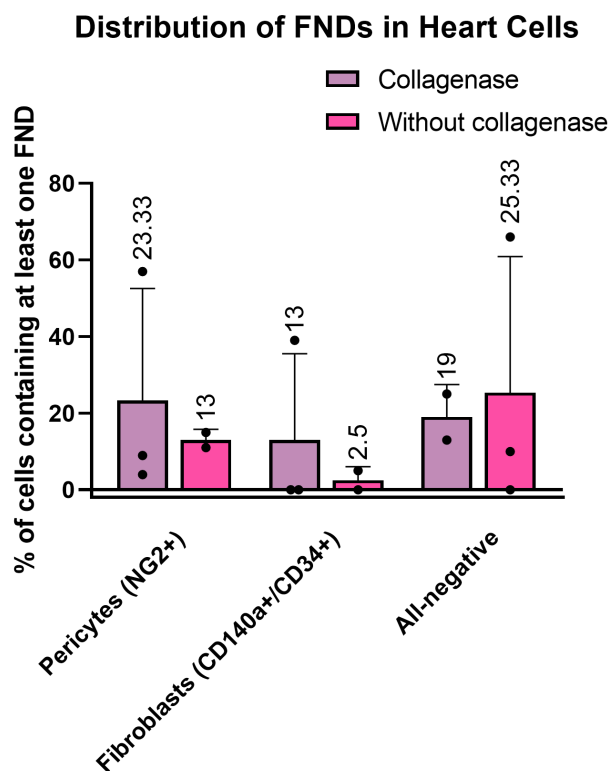


**Figure 16.** Distribution of FNDs among FACS-sorted cells from the heart. Each data point represents the percentage of cells containing at least one FND. Data from three animals is included. Bars indicate the mean percentage (displayed above each bar), and error bars represent the standard deviation. For all cell types, collagenase pre-treatment increases FND uptake. The majority of FNDs are taken up by "all-negative" cells and pericytes.

Table 3: Distribution of FNDs among different FACS-sorted heart cell types. The table presents the total number of cells counted, the number of cells with FNDs, and the percentage of cells with FNDs for each cell type and "all-negative" category. Data are shown for samples with and without collagenase pre-treatment. Samples were taken from three animals, however, not all cell types were sorted in each sample. (Continued)

|  |  |  |  |  |
|---|---|---|---|---|
|  |  |  | 3* | 0 | 0 |
|  |  | No | 6* | 0 | 0 |
|  |  |  | 100 | 5 | 5 |
|  |  | Yes | 8* | 2 | 25 |
|  |  |  | 8* | 1 | 13 |
| *All-negative* |  |  | 0* | 0 | 0 |
|  |  | No | 100 | 10 | 10 |
|  |  |  | 35* | 23 | 66 |

\* Instances where the full cell count of 100 cells was not attainable

# 4 Discussion

This research investigates the antioxidant effects of OBE100 in models of aging and hepatic steatosis, including positive control animals for the latter, hypothesizing a reduction in free radicals after 6, 24, and 48-hour incubation periods. Additionally, it explores the application of nanodiamond-based quantum sensing in tissues, a novel achievement, and its potential for testing antioxidant drugs in liver tissue. Moreover, the study aims to refine this methodology by enhancing the understanding of FND distribution within tissues.

## 4.1 Temporal Reduction of Free Radicals by OBE100 in Naturally Aged Mice

The lack of a statistically significant difference between the two baseline measurements (Figure 5) suggests that, in the absence of OBE100 treatment, there are no changes in T1 values or free radical levels. This observation indicates that the subsequent effects can be attributed to OBE100, thereby ruling out the influence of other factors like natural tissue regeneration.

The statistically significant increase in T1 values after 24-hour incubation with OBE100, compared to the baseline (Figure 5), suggests a reduction in free radicals and underscores the antioxidant potential of OBE100. This finding aligns with research by Acin et al. (2021), which highlights OBE100's capacity to mitigate oxidative stress in conditions like obesity and insulin resistance, specifically noting its ability to decrease ROS. Conversely, the absence of a statistically significant reduction in free radicals following the 6-hour incubation indicates that the antioxidant effect of OBE100 manifests only after 24 hours.

The lack of significance in the 6-hour incubation period may also be attributed to factors such as an insufficient number of animal models or measurements per animal, contributing to data variability.

The reduction in T1 values after 48-hour continuous incubation with OBE100 indicates an increase in free radicals (Figure 5). Viability assessment has not indicated compromised tissue viability (Section 4.5.2), suggesting that this phenomenon cannot be attributed to any detrimental effects of the extract. It is hypothesized that the accumulation of free radicals could result from a decline in OBE100's antioxidant activity after 24 hours, which could potentially be mitigated by administering an additional dose of the extract. This approach mirrors the common practice in intraperitoneal drug administration, as seen with drugs like mitomycin C, which are administered in multiple doses to maintain consistent drug concentrations (de Bree et al., 2017). This hypothesis is further explored in both positive control and fatty-acid-induced mice (Section 4.2 and 4.3).

## 4.2 Effect of Additional Dose of OBE100 on Free Radical Reduction in Positive Control Mice

For 12-week-old mice, continuous incubation with OBE100 over varying durations does not yield statistically significant differences compared to the 24-hour baseline measurement. However, administering an additional dose of OBE100 after the initial 24-hour incubation leads to a significant reduction in free radicals, confirming our hypothesis. To discern the impact of

OBE100 versus the medium change on the reduction in free radicals, we applied the same medium change for the 48-hour baseline measurement. This condition showed no significant difference compared to the 24-hour baseline (Figure 6), affirming that the observed effect is solely due to OBE100. These findings highlight OBE100's pronounced antioxidant potential even under non-stress conditions (young animals without fatty acid treatment), particularly when an additional dose of the extract is administered after the initial 24 hours.

Further investigation aims to determine if this effect persists under physiological stressors, such as hepatic steatosis induced by fatty acid treatment.

## 4.3 Antioxidant Efficacy of OBE100 under Hepatic Steatosis Conditions

A marked decrease in T1 values is observed in 12-week-old mice following fatty acid treatment, indicating an increase in free radicals. This outcome is anticipated, as fatty acid treatment mimics hepatic steatosis, a condition closely linked to heightened oxidative stress levels (Rabelo et al., 2024). To examine tissue responses following fatty acid treatment in the absence of OBE100, PCLS were incubated for either 24 or 48 hours in WEGG medium. The lack of statistically significant differences between these conditions and the initial fatty acid measurement indicates that no tissue recovery occurs during this period (Figure 7). This underscores that the observed effects are solely attributable to OBE100.

After a 48-hour incubation with OBE100, including an additional dose, a highly statistically significant decrease in free radicals is observed, similar to findings in positive control mice. Importantly, the T1 value shows no statistically significant difference compared to the baseline measurement before the fatty acid treatment (Figure 7), indicating a complete return of free radical levels to the pre-steatotic state. This demonstrates OBE100's antioxidant potential under conditions mimicking hepatic steatosis. Previous research supports these findings, demonstrating that OBE100 exhibits hypolipemic activities (Bentancur et al., 2021). Studies indicate that mitigating oxidative stress through lipid-lowering interventions can restore the body's antioxidant capacity by decreasing the rate of lipid peroxidation, potentially preventing or delaying further disease development (Aikawa et al., 2002; Yang et al., 2008). Our findings position OBE100 as a promising candidate for managing diseases associated with a steatotic liver. The lack of statistically significant decreases in free radicals after 6 and 24 hours of incubation (Figure 7) further emphasizes that OBE100 achieves its full antioxidant potential with a delay and benefits from an additional dose.

## 4.4 Validation of Hypolipemic Activity of OBE100

Following fatty acid treatment, as anticipated, a highly statistically significant increase in triglyceride levels in PCLS is observed (Figure 8). This confirms that the fatty acid treatment effectively increased fat accumulation within hepatocytes, leading to hepatic steatosis. These conditions validate the setup for OBE100 treatment in fatty acid-induced mice and triglyceride estimation.

OBE100, with or without collagenase, significantly decreases triglyceride levels after 48 hours of incubation. This reduction aligns with the significant decrease in free radicals in fatty acid-induced mice, reaffirming the hypolipemic activity of OBE100 and suggesting that it may

underlie the antioxidant potential of OBE100, as noted above (Section 4.3).

With collagenase pre-treatment, a reduction in triglyceride levels becomes evident only after 48 hours of incubation with OBE100, contrasting with the hypolipemic effect observed as early as 6 hours in PCLS without collagenase treatment (Figure 8, b). Additionally, this effect is less pronounced in the collagenase-treated samples (Figure 8, a). Previous research has demonstrated that disrupting the extracellular matrix (ECM) collagen barrier with *in situ* collagenase enhances drug penetration in tissues, thereby improving therapeutic efficacy (Fan et al., 2020; J. Li et al., 2018; Wang et al., 2024). Our findings diverge from this perspective. Furthermore, we found no statistically significant differences in triglyceride levels between PCLS with and without collagenase pre-treatment after fatty acid treatment, before OBE100 incubation (Figure 9). This suggests that collagenase does not inhibit fat accumulation. Overall, our results indicate a potential interaction between OBE100 and collagenase, warranting further investigation.

## 4.5 Viability Assesment

### 4.5.1 OBE100 Concentration, Incubation With FNDs, Collagenase Pre-treatment

No significant decrease in viability is observed for various OBE100 concentrations, FND treatment, or collagenase treatment, confirming the experimental choices employed. Particularly, the use of OBE100 at 100 μg/mL is validated, as the observed decrease with increasing concentration is not statistically significant (Figure 10, a). Given that these PCLS were exposed to a 48-hour incubation at 100 μg/mL, the longest duration employed with OBE100 in this study, and exhibited no viability reduction beyond acceptable limits, this outcome substantiates that the observed trend of declining viability with prolonged OBE100 incubation across positive control and fatty-acid-induced animal models (Section 4.5.3 and 4.5.4) likely stems from the extended pre-cryopreservation incubation of these PCLS rather than the extract itself. Despite PCLS typically maintaining ATP content for up to 72 hours, the experimental timeline surpassed this threshold (I. A. de Graaf et al., 2010).

The reduction in viability after collagenase pre-treatment (Figure 10, b) can be explained by collagenase's role as a proteinase that cleaves type I and III collagens in the liver, leading to the disintegration of liver tissue (Poole et al., 1995; Seaman et al., 2015; Voss et al., 1980).

### 4.5.2 OBE100 Treatment in Naturally Aged Mice

For PCLS from the naturally aged mice model, no statistically significant difference is found among the means of different experimental conditions, confirming the validity of the experimental setup (Figure 11).

Notably, no significant difference is observed between incubation with FNDs alone and incubation with FNDs for various durations with OBE100, suggesting that the incubation with the extract does not adversely affect tissue viability. However, a trend of declining ATP/Protein ratio values is observed as incubation time with OBE100 progresses (Figure 11, a). This decline may be attributed to the extended incubation periods before cryopreservation, as outlined in Section 4.5.1. However, since no additional dose of OBE100 was administered after the initial 24 hours of incubation, the findings discussed therein do not fully substantiate this hypothesis.

Nonetheless, given that the decline is statistically insignificant, it can be concluded that PCLS retain their viability after incubation with OBE100.

The lack of a statistically significant difference between the T1 measurements at the 24-hour baseline and those after various durations of incubation with OBE100 (Figure 13, b), indicates consistency in the execution of nanodiamond-based quantum sensing measurements throughout the experiment.

The detected decrease in ATP/Protein ratio when contrasting PCLS following diverse incubation periods with OBE100 and FNDs against those after the same incubation periods but post-T1 measurements (Figure 11, c) may be ascribed to the limited viability of the tissue. Typically, tissue viability endures merely 30 minutes outside the incubator before cellular degeneration initiates, which coincides with the measurement timeframe (Nussbaum et al., 2022; Rodriguez, 1991). The absence of a statistically significant decline confirms that PCLS maintained their viability within an acceptable range following T1 measurements.

### 4.5.3  OBE100 Treatment in Positive Control Mice

For the PCLS from the 12-week-old positive control mice, no statistically significant difference is observed between various incubation times with OBE100 and FNDs, and the 24-hour incubation with FNDs without OBE100 (Figure 12, a). This, along with the fact that the employed concentration (100 µg/mL) does not decrease viability below acceptable margins (Section 4.5.1), validates the use of OBE100 in these conditions.

The absence of statistically significant differences between the 24-hour baseline and T1 measurements obtained following different incubation periods with OBE100 (Figure 12, b) underscores the reliability of nanodiamond-based quantum sensing measurements throughout the study.

The statistically significant decline in the ATP/Protein ratio in PCLS after T1 measurements, compared to both the 6 and 24-hour incubations with OBE100 following FND incubation, may be attributed to limitations in tissue viability, as discussed in the section on naturally aged animal models (Section 4.5.2). Additionally, the prolonged incubation before cryopreservation likely contributes to this decline. This explains why the 48-hour incubation with OBE100 does not show a statistically significant difference compared to PCLS incubated under the same conditions after T1 measurements, as tissue viability may have already been slightly reduced by then (Figure 12, c). Despite this significant decrease in viability, it is crucial to emphasize the extract's continued efficacy in reducing free radicals.

### 4.5.4  OBE100 Treatment in Fatty Acid-Induced Mice

For the PCLS from the fatty-acid-induced mice model mimicking hepatic steatosis, no statistically significant differences are observed between means of different experimental conditions, thereby validating the experimental setup (Figure 13).

An increase in the ATP/Protein ratio, although not statistically significant, is observed between PCLS collected before any treatment on the slicing day and those after 24-hour incubation with FNDs prior to fatty acid treatment. Given that FNDs have not previously been shown to affect tissue viability (Section 4.5.1), this increase likely stems from the pre-incubation phase before cryopreservation. In our study, UW solution was employed to store livers until

further processing post-removal from mice and to wash PCLS after collagenase pre-treatment. Research by I. de Graaf et al. (2002) has shown that using UW solution during these stages reduces the vulnerability of liver slices to damage from rapid freezing, a common method of cryopreservation, which leads to viability loss. This indicates that using UW solution allows PCLS to maintain their restored physiological homeostasis achieved through pre-incubation. This observation may also account for the non-significant increase in tissue viability noted after a 48-hour incubation in WEGG medium without any treatment compared to the initial post-slicing conditions. Overall, this finding affirms that the tissue's viability is sustained prior to the introduction of OBE100.

The decline in viability after the fatty acid treatment (Figure 13, a) could be attributed to oxidative stress, which damages cellular components such as DNA, lipids, and proteins (Ray et al., 2012). Based on the results of the viability assessment, it can be inferred that the PCLS retained their viability within acceptable margins following the fatty acid treatment.

Since no statistically significant differences are observed between the 24-hour baseline and T1 measurements following various incubation periods with OBE100 (Figure 13, b), the consistency of nanodiamond-based quantum sensing measurements throughout the study is validated.

The observed decrease in the ATP/Protein ratio when comparing PCLS after various incubation periods with OBE100 and FNDs to those after the same incubation periods but post-T1 measurements (Figure 13, c) may be attributed to the limited viability of the tissue, as discussed in the section on naturally aged animal models above (Section 4.5.2). Since this difference lacks statistical significance, the viability of PCLS post-T1 measurements is confirmed.

## 4.6 Distribution of Fluorescent Nanodiamonds

### 4.6.1 Collagenase Pre-Treatment Reduces FND Uptake in Macrophages Despite Increasing Uptake in Other Cell Types

In all three organs, except for macrophages and the "all-negative" category (which includes all FACS-sorted cells negative for the used cell markers and thus difficult to analyze), collagenase pre-treatment enhances FND uptake. Previous studies have shown that the ECM collagen barrier limits cellular uptake of nanocarriers and therapeutic agents. Degrading this barrier with collagenase, a $Zn^{2+}$-dependent matrix metalloproteinase that cleaves peptide bonds in collagen (Patel et al., 2023), has been demonstrated to increase their uptake (Eikenes et al., 2004; Henke et al., 2020; Mai et al., 2024; Wang et al., 2018; L. Zhou et al., 2022). Additionally, both collagenase type I and type II used in this research exhibit trypsin-like activity, and treating cell clusters with trypsin has been shown to increase FND uptake (Sigaeva, 2022).

In both splenic and kidney cells, collagenase pre-treatment reduces macrophage uptake of FNDs. This finding is notable as it challenges the conventional notion that collagenase enhances cellular uptake. However, it is important to note that a full count of 100 cells was not feasible for splenic macrophages, and for kidney macrophages, this was also not attainable in two out of six samples (Table 1 and 2). Nevertheless, this reduction in uptake following collageanse treatment is observed in both organs. The discrepancy may arise from the diverse phenotypes and functions that macrophages exhibit in response to microenvironmental cues (Van Overmeire et al., 2014). A study by Vasse et al. (2023) indicates that macrophages, particularly in the presence of collagen type I, which is abundant in the kidney and spleen (Hanadhita et al.,

2019; Rasmussen et al., 2019), upregulate the expression of the mannose receptor CD206. This receptor is involved in phagocytosis, a process implicated in the uptake of FNDs (Niora et al., 2023; Prabhakar et al., 2017; Tanaka et al., 2021; Wright et al., 2021).

### 4.6.2 Distribution of FNDs in Spleen

In the spleen, macrophages without collagenase pre-treatment exhibit the highest levels of FND internalization (Figure 14), attributed to their well-researched phagocytic capabilities (Han et al., 2016).

B cells exhibit the second highest uptake of FNDs (Figure 14), consistent with research indicating that follicular B cells, capable of entering lymphoid follicles in the spleen (Loder et al., 1999), display phagocytic activity akin to specialized antigen-presenting cells such as macrophages and dendritic cells. This phagocytic activity is mediated by RhoG GTPase, which participates in the engulfment of apoptotic bodies and phagocytosis dependent on Fc receptors for Immunoglobulin G (Fc$\gamma$R) and complement receptor 3 (CR3) in macrophages (Martinez-Riaao et al., 2018).

The low FND uptake observed in T cells (Figure 14) can be attributed to their non-phagocytic nature (Narni-Mancinelli et al., 2011).

### 4.6.3 Distribution of FNDs in Kidney

As in the spleen, macrophages in the kidney without collagenase pre-treatment exhibit the highest levels of FND uptake, attributed to their phagocytic abilities (Han et al., 2016). Conversely, other cell types also demonstrate relatively high levels of FND internalization. Endothelial cells (CD34+), as non-professional phagocytes, possess a limited capacity for engulfing target particles due to the absence of specific receptors for phagocytosis. However, they actively participate in the clearance of apoptotic cells (Calvert & Ryan, 2023; Ji et al., 2020; Sihombing et al., 2021). This characteristic may explain their comparatively lower uptake of FNDs compared to macrophages lacking collagenase treatment. Podocytes (Podoplanin+), a type of glomerular epithelial cell (Maezawa et al., 2013), exhibit FND internalization levels similar to those of endothelial cells (Figure 15). This finding aligns with previous research by Goldwich et al. (2013), which concluded that podocytes, akin to macrophages, function as professional antigen-presenting cells and demonstrate significant phagocytic activity both in vitro and in vivo. Nevertheless, it is important to note that in two podocyte samples, achieving a full cell count was not feasible, resulting in very few cells being counted, and there is a considerable variability in the results (Table 2). However, the findings are relatively consistent within the same animal, both with and without collagenase treatment, across all samples.

### 4.6.4 Distribution of FNDs in Heart

In the heart, pericytes — mural cells that cover microvascular capillaries (Su et al., 2021) — initially exhibit low uptake of FNDs, with a slight increase following collagenase treatment (Figure 16). While the phagocytic capabilities of cardiac pericytes remain unclear, research on brain pericytes indicates that they ingest small molecules and soluble substances through various forms of endocytosis. Since pericyte density varies across different tissues, suggesting

specialized functions in different organs, this alone is not sufficient to conclude the level of phagocytic activity of cardiac pericytes (Bergers & Song, 2005; Z.-S. Zhang et al., 2020).

Cardiac fibroblasts display minimal internalization of FNDs (Figure 16), which is unexpected given their characterization as non-professional phagocytes (DeBerge et al., 2017). It is noteworthy that conducting a complete cell count was challenging; it was feasible in only two out of five cases (including both collagenase-treated and untreated samples), with fewer than 10 cells counted per sample in the remaining cases, where detectable diamonds were rarely observed (Table 3). This limited cell count likely contributes to the observed low FND uptake.

## 4.7 Limitations

Nanodiamond-based quantum sensing used for free radical detection is not capable of differentiating between ROS and RNS. However, ROS and RNS display distinct chemical properties and biological activities, arising from different pathways and varying reactivity with biomolecules (Di Meo et al., 2016; Lushchak & Lushchak, 2021; Yilmaz et al., 2017). This limitation could hinder the comprehensive characterization of OBE100's antioxidant effects.

In nanodiamond-based quantum sensing and subsequent viability and triglyceride assessments, three or four mouse models were utilized. For evaluating the distribution of FNDs, only two to three animal models were employed, whereas for assessing the viability of PCLS under varying OBE100 concentrations, only one mouse model was used. Given the relatively high data dispersion observed, increasing the number of animal models would be advisable. This would improve the robustness of the findings and ensure a broader coverage of biological variability and trends.

## 4.8 Conclusion and Future Perspectives

OBE100 demonstrates robust antioxidant potential in models of aging, hepatic steatosis, and under normal physiological conditions, confirming our initial hypothesis. The onset of action is delayed, manifesting at 24 hours in naturally aged mice and 48 hours in both fatty acid-induced and positive control animals. Notably, in naturally aged mice, the antioxidant efficacy of OBE100 diminishes after 24 hours of incubation; however, administering an additional dose post-initial 24-hour period proved effective, as validated in subsequent animal models.

In mice with fatty acid-induced hepatic steatosis, OBE100 effectively restores free radical levels to their pre-steatotic state. This finding is substantiated by triglyceride estimation, which confirms OBE100's hypolipemic effect and its correlation with the reduction in free radicals observed after 48 hours of incubation. Moreover, the hypolipemic effect manifests earlier and is more pronounced in samples without collagenase pre-treatment, suggesting a potential interaction between OBE100 and collagenase that warrants further investigation.

Viability assays demonstrate no adverse effects of OBE100, FND incubation, or collagenase pretreatment on PCLS health. Experimental conditions are validated for both naturally aged and fatty acid-induced mice. However, decreased viability is noted in positive control mice following nanodiamond-based quantum sensing measurements for free radical assessment. Despite this, OBE100 continues to exhibit antioxidant activity in these conditions.

Thus, OBE100 emerges as a promising candidate for managing oxidative stress associated

with diseases such as steatotic liver and aging - two conditions urgently requiring effective treatments. Further exploration of its impact on gene expression through RNA analysis could provide deeper insights into its underlying molecular mechanisms, although detailed analysis of collected samples exceeds the current scope of this study.

Additionally, this research highlights nanodiamond-based quantum sensing as an innovative tool for effectively assessing free radical generation in tissue slices. The study enhances our understanding of FND cellular uptake and distribution within tissues: in splenic cells, FNDs are predominantly found in macrophages, with fewer in B cells and 'all-negative' cells, and almost none in T cells. In the kidney, FND uptake is high in macrophages and other cells, whereas heart cells show the lowest internalization, with pericytes and 'all-negative' cells exhibiting the highest uptake, and fibroblasts demonstrating minimal uptake. However, most fibroblast samples counted fewer than 10 cells. Despite the general understanding that collagenase increases cellular uptake, this phenomenon does not hold for macrophages. Similar trends were observed in both kidney and spleen samples, though complete cell counts were not feasible in all instances. These insights into the distribution and uptake of FNDs across different cell types have the potential to guide future applications in research methodologies.

# References

Abbott, R. D., & Kaplan, D. L. (2015). Strategies for improving the physiological relevance of human engineered tissues. *Trends in Biotechnology*, *33*(7), 401–407. https://doi.org/10.1016/j.tibtech.2015.04.003

Acin, S., Munoz, D. L., Guillen, A., Soscue, D., Castano, A., Echeverri, F., & Balcazar, N. (2021). Triterpene-enriched fractions from eucalyptus tereticornis ameliorate metabolic alterations in a mouse model of diet-induced obesity. *Journal of Ethnopharmacology*, *265*, 113298. https://doi.org/10.1016/j.jep.2020.113298

Aikawa, M., Sugiyama, S., Hill, C. C., Voglic, S. J., Rabkin, E., Fukumoto, Y., Schoen, F. J., Witztum, J. L., & Libby, P. (2002). Lipid lowering reduces oxidative stress and endothelial cell activation in rabbit atheroma. *Circulation*, *106*(11), 1390–1396. https://doi.org/10.1161/01.cir.0000028465.52694.9b

Alhasawi, A., Legendre, F., Jagadeesan, S., Appanna, V., & Appanna, V. (2019). Biochemical strategies to counter nitrosative stress. *Microbial Diversity in the Genomic Era*, 153–169. https://doi.org/10.1016/b978-0-12-814849-5.00010-1

Arroyave-Ospina, J. C., Wu, Z., Geng, Y., & Moshage, H. (2021). Role of oxidative stress in the pathogenesis of non-alcoholic fatty liver disease: Implications for prevention and therapy. *Antioxidants*, *10*(2), 174. https://doi.org/10.3390/antiox10020174

Bajerski, F., Stock, J., Hanf, B., Darienko, T., Heine-Dobbernack, E., Lorenz, M., Naujox, L., Keller, E. R., Schumacher, H. M., Friedl, T., & et al. (2018). Atp content and cell viability as indicators for cryostress across the diversity of life. *Frontiers in Physiology*, *9*. https://doi.org/10.3389/fphys.2018.00921

Balakumar, P., Rohilla, A., & Thangathirupathi, A. (2010). Gentamicin-induced nephrotoxicity: Do we have a promising therapeutic approach to blunt it? *Pharmacological Research*, *62*(3), 179–186. https://doi.org/10.1016/j.phrs.2010.04.004

Bartucci, R., Åberg, C., Melgert, B. N., Boersma, Y. L., Olinga, P., & Salvati, A. (2020). Time-resolved quantification of nanoparticle uptake, distribution, and impact in precision-cut liver slices. *Small*, *16*(21). https://doi.org/10.1002/smll.201906523

Basu, S., Campbell, H. M., Dittel, B. N., & Ray, A. (2010). Purification of specific cell population by fluorescence activated cell sorting (facs). *Journal of Visualized Experiments*, (41). https://doi.org/10.3791/1546

Bentancur, L. I., Munoz, D. L., Guillen, A., Echeverri, L. F., Balcazar, N., & Acin, S. (2021). Major triterpenoids from eucalyptus tereticornis have enhanced beneficial effects in cellular models when mixed with minor compounds present in raw extract. *Anais da Academia Brasileira de Ciencias*, *93*(suppl 3). https://doi.org/10.1590/0001-3765202120201351

Bergers, G., & Song, S. (2005). The role of pericytes in blood-vessel formation and maintenance. *Neuro-Oncology*, *7*(4), 452–464. https://doi.org/10.1215/s1152851705000232

Bokkon, I. (2012). Editorial (hot topic: Recognition of functional roles of free radicals). *Current Neuropharmacology*, *10*(4), 287–288. https://doi.org/10.2174/157015912804499474

Calvert, B. A., & Ryan, A. L. (2023). Non-myeloid cell phagocytosis. *Phagocytosis - Main Key of Immune System*. https://doi.org/10.5772/intechopen.110583

Chen, Z., Tian, R., She, Z., Cai, J., & Li, H. (2020). Role of oxidative stress in the pathogenesis of nonalcoholic fatty liver disease. *Free Radical Biology and Medicine*, *152*, 116–141. https://doi.org/10.1016/j.freeradbiomed.2020.02.025

Damle, V., Wu, K., Arouri, D., & Schirhagl, R. (2022). Detecting free radicals post viral infections. *Free Radical Biology and Medicine*, *191*, 8–23. https://doi.org/10.1016/j.freeradbiomed.2022.08.013

DeBerge, M., Zhang, S., Glinton, K., Grigoryeva, L., Hussein, I., Vorovich, E., Ho, K., Luo, X., & Thorp, E. B. (2017). Efferocytosis and outside-in signaling by cardiac phagocytes. links to repair, cellular programming, and intercellular crosstalk in heart. *Frontiers in Immunology*, *8*. https://doi.org/10.3389/fimmu.2017.01428

de Bree, E., Michelakis, D., Stamatiou, D., Romanos, J., & Zoras, O. (2017). Pharmacological principles of intraperitoneal and bidirectional chemotherapy. *Pleura and Peritoneum*, *2*(2), 47–62. https://doi.org/10.1515/pp-2017-0010

de Graaf, I., Geerlinks, A., & Koster, H. (2002). Incubation at 37°c prior to cryopreservation decreases viability of liver slices after cryopreservation by rapid freezing. *Cryobiology*, *45*(1), 1–9. https://doi.org/10.1016/s0011-2240(02)00101-3

de Graaf, I. A., Olinga, P., de Jager, M. H., Merema, M. T., de Kanter, R., van de Kerkhof, E. G., & Groothuis, G. M. (2010). Preparation and incubation of precision-cut liver and intestinal slices for application in drug metabolism and toxicity studies. *Nature Protocols*, *5*(9), 1540–1551. https://doi.org/10.1038/nprot.2010.111

Dewyse, L., Reynaert, H., & van Grunsven, L. A. (2021). Best practices and progress in precision-cut liver slice cultures. *International Journal of Molecular Sciences*, *22*(13), 7137. https://doi.org/10.3390/ijms22137137

Di Meo, S., Reed, T. T., Venditti, P., & Victor, V. M. (2016). Role of ros and rns sources in physiological and pathological conditions. *Oxidative Medicine and Cellular Longevity*, *2016*, 1–44. https://doi.org/10.1155/2016/1245049

Dikalov, S. I., & Harrison, D. G. (2014). Methods for detection of mitochondrial and cellular reactive oxygen species. *Antioxidants amp; Redox Signaling*, *20*(2), 372–382. https://doi.org/10.1089/ars.2012.4886

Eikenes, L., Bruland, Ø. S., Brekken, C., & Davies, C. d. (2004). Collagenase increases the transcapillary pressure gradient and improves the uptake and distribution of monoclonal antibodies in human osteosarcoma xenografts. *Cancer Research*, *64*(14), 4768–4773. https://doi.org/10.1158/0008-5472.can-03-1472

Fabbrini, E., Sullivan, S., & Klein, S. (2009). Obesity and nonalcoholic fatty liver disease: Biochemical, metabolic, and clinical implications. *Hepatology*, *51*(2), 679–689. https://doi.org/10.1002/hep.23280

Fan, Q.-Q., Zhang, C.-L., Qiao, J.-B., Cui, P.-F., Xing, L., Oh, Y.-K., & Jiang, H.-L. (2020). Extracellular matrix-penetrating nanodrill micelles for liver fibrosis therapy. *Biomaterials*, *230*, 119616. https://doi.org/10.1016/j.biomaterials.2019.119616

Gambino, R., Musso, G., & Cassader, M. (2011). Redox balance in the pathogenesis of nonalcoholic fatty liver disease: Mechanisms and therapeutic opportunities. *Antioxidants amp; Redox Signaling*, *15*(5), 1325–1365. https://doi.org/10.1089/ars.2009.3058

Gargiulo, S., Greco, A., Gramanzini, M., Petretta, M. P., Ferro, A., Larobina, M., Panico, M., Brunetti, A., & Cuocolo, A. (2012). Pet/ct imaging in mouse models of myocardial ischemia. *Journal of Biomedicine and Biotechnology*, *2012*, 1–12. https://doi.org/10.1155/2012/541872

Goldwich, A., Burkard, M., Ölke, M., Daniel, C., Amann, K., Hugo, C., Kurts, C., Steinkasserer, A., & Gessner, A. (2013). Podocytes are nonhematopoietic professional antigen-presenting cells. *Journal of the American Society of Nephrology*, *24*(6), 906–916. https://doi.org/10.1681/asn.2012020133

Han, C. Z., Juncadella, I. J., Kinchen, J. M., Buckley, M. W., Klibanov, A. L., Dryden, K., Onengut-Gumuscu, S., Erdbrügger, U., Turner, S. D., Shim, Y. M., & et al. (2016). Macrophages redirect phagocytosis by non-professional phagocytes and influence inflammation. *Nature*, *539*(7630), 570–574. https://doi.org/10.1038/nature20141

Hanadhita, D., Rahma, A., Wahid, M. R., Mayasari, N. L., Satyaningtijas, A. S., Hondo, E., & Agungpriyono, S. (2019). Extracellular matrix composition of different spleen compartments of fruit bats. *Anatomia, Histologia, Embryologia*, *49*(2), 281–289. https://doi.org/10.1111/ahe.12526

Hemelaar, S. R., de Boer, P., Chipaux, M., Zuidema, W., Hamoh, T., Martinez, F. P., Nagl, A., Hoogenboom, J. P., Giepmans, B. N., & Schirhagl, R. (2017). Nanodiamonds as multi-purpose labels for microscopy. *Scientific Reports*, *7*(1). https://doi.org/10.1038/s41598-017-00797-2

Henke, E., Nandigama, R., & Ergün, S. (2020). Extracellular matrix in the tumor microenvironment and its impact on cancer therapy. *Frontiers in Molecular Biosciences*, *6*. https://doi.org/10.3389/fmolb.2019.00160

Herzenberg, L. A., De Rosa, S. C., & Herzenberg, L. A. (2000). Monoclonal antibodies and the facs: Complementary tools for immunobiology and medicine. *Immunology Today*, *21*(8), 383–390. https://doi.org/10.1016/s0167-5699(00)01678-9

Houldsworth, A. (2023). Role of oxidative stress in neurodegenerative disorders: A review of reactive oxygen species and prevention by antioxidants. *Brain Communications*, *6*(1). https://doi.org/10.1093/braincomms/fcad356

Idilman, I. S., Ozdeniz, I., & Karcaaltincaba, M. (2016). Hepatic steatosis: Etiology, patterns, and quantification. *Seminars in Ultrasound, CT and MRI*, *37*(6), 501–510. https://doi.org/10.1053/j.sult.2016.08.003

Institute of Medicine (US) Committee on the Future Health Care Workforce for Older Americans. (2008). *Health status and health care service utilization*. National Academies Press.

Jakubczyk, K., Dec, K., Kaldunska, J., Kawczuga, D., Kochman, J., & Janda, K. (2020). Reactive oxygen species - sources, functions, oxidative damage. *Polski merkuriusz lekarski : organ Polskiego Towarzystwa Lekarskiego*, *48 284*, 124–127. https://api.semanticscholar.org/CorpusID:218470982

Ji, S., Dong, W., Qi, Y., Gao, H., Zhao, D., Xu, M., Li, T., Yu, H., Sun, Y., Ma, R., & et al. (2020). Phagocytosis by endothelial cells inhibits procoagulant activity of platelets of essential thrombocythemia in vitro. *Journal of Thrombosis and Haemostasis*, *18*(1), 222–233. https://doi.org/10.1111/jth.14617

Katerji, M., Filippova, M., & Duerksen-Hughes, P. (2019). Approaches and methods to measure oxidative stress in clinical samples: Research applications in the cancer field. *Oxidative Medicine and Cellular Longevity*, *2019*, 1–29. https://doi.org/10.1155/2019/1279250

Knight, J. A. (2000). Review: Free radicals, antioxidants, and the immune system. *Annals of clinical and laboratory science*, *30 2*, 145–58. https://api.semanticscholar.org/CorpusID:30301640

Kokkorakis, M., Muzurovic, E., Volcansek, S., Chakhtoura, M., Hill, M. A., Mikhailidis, D. P., & Mantzoros, C. S. (2024). Steatotic liver disease: Pathophysiology and emerging pharmacotherapies. *Pharmacological Reviews*, *76*(3), 454–499. https://doi.org/10.1124/pharmrev.123.001087

Lazarus, J. V., Mark, H. E., Anstee, Q. M., Arab, J. P., Batterham, R. L., Castera, L., Cortez-Pinto, H., Crespo, J., Cusi, K., Dirac, M. A., & et al. (2021). Advancing the global public health agenda for nafld: A consensus statement. *Nature Reviews Gastroenterology amp; Hepatology*, *19*(1), 60–78. https://doi.org/10.1038/s41575-021-00523-4

Levine, R. L., Garland, D., Oliver, C. N., Amici, A., Climent, I., Lenz, A.-G., Ahn, B.-W., Shaltiel, S., & Stadtman, E. R. (1990). [49] determination of carbonyl content in oxidatively modified proteins. *Oxygen Radicals in Biological Systems Part B: Oxygen Radicals and Antioxidants*, 464–478. https://doi.org/10.1016/0076-6879(90)86141-h

Li, J., Xie, C., Huang, J., Jiang, Y., Miao, Q., & Pu, K. (2018). Semiconducting polymer nanoenzymes with photothermic activity for enhanced cancer therapy. *Angewandte Chemie International Edition*, *57*(15), 3995–3998. https://doi.org/10.1002/anie.201800511

Li, R., Vedelaar, T., Mzyk, A., Morita, A., Padamati, S. K., & Schirhagl, R. (2022). Following polymer degradation with nanodiamond magnetometry. *ACS Sensors*, *7*(1), 123–130. https://doi.org/10.1021/acssensors.1c01782

Li, Y. R., & Trush, M. (2016). Defining ros in biology and medicine. *Reactive Oxygen Species*, *1*(1). https://doi.org/10.20455/ros.2016.803

Lobo, V., Patil, A., Phatak, A., & Chandra, N. (2010). Free radicals, antioxidants and functional foods: Impact on human health. *Pharmacognosy Reviews*, *4*(8), 118. https://doi.org/10.4103/0973-7847.70902

Loder, B. F., Mutschler, B., Ray, R. J., Paige, C. J., Sideras, P., Torres, R., Lamers, M. C., & Carsetti, R. (1999). B cell development in the spleen takes place in discrete steps and is determined by the quality of b cell receptor–derived signals. *The Journal of Experimental Medicine*, *190*(1), 75–90. https://doi.org/10.1084/jem.190.1.75

Longobardi Givan, A. (2001). Instrumentation: Into the black box. *Flow Cytometry: First Principles*, 15–39. https://doi.org/10.1002/0471223948.ch3

Loomba, R., & Sanyal, A. J. (2013). The global nafld epidemic. *Nature Reviews Gastroenterology amp; Hepatology*, *10*(11), 686–690. https://doi.org/10.1038/nrgastro.2013.171

Lopez-Otin, C., Blasco, M. A., Partridge, L., Serrano, M., & Kroemer, G. (2013). The hallmarks of aging. *Cell*, *153*(6), 1194–1217. https://doi.org/10.1016/j.cell.2013.05.039

Lopez-Otin, C., Blasco, M. A., Partridge, L., Serrano, M., & Kroemer, G. (2023). Hallmarks of aging: An expanding universe. *Cell*, *186*(2), 243–278. https://doi.org/10.1016/j.cell.2022.11.001

Lopez-Otin, C., Galluzzi, L., Freije, J. M., Madeo, F., & Kroemer, G. (2016). Metabolic control of longevity. *Cell*, *166*(4), 802–821. https://doi.org/10.1016/j.cell.2016.07.031

Lushchak, V. I., & Lushchak, O. (2021). Interplay between reactive oxygen and nitrogen species in living organisms. *Chemico-Biological Interactions*, *349*, 109680. https://doi.org/10.1016/j.cbi.2021.109680

Maezawa, Y., Cina, D., & Quaggin, S. E. (2013). Glomerular cell biology. *Seldin and Giebisch's The Kidney*, 721–755. https://doi.org/10.1016/b978-0-12-381462-3.00022-7

Mai, Z., Lin, Y., Lin, P., Zhao, X., & Cui, L. (2024). Modulating extracellular matrix stiffness: A strategic approach to boost cancer immunotherapy. *Cell Death amp; Disease*, *15*(5). https://doi.org/10.1038/s41419-024-06697-4

Martinez-Reyes, I., & Cuezva, J. M. (2014). The h+-atp synthase: A gate to ros-mediated cell death or cell survival. *Biochimica et Biophysica Acta (BBA) - Bioenergetics*, *1837*(7), 1099–1112. https://doi.org/10.1016/j.bbabio.2014.03.010

Martinez-Riaao, A., Bovolenta, E. R., Mendoza, P., Oeste, C. L., Martin-Bermejo, M. J., Bovolenta, P., Turner, M., Martinez-Martin, N., & Alarcon, B. (2018). Antigen phagocytosis by b cells is required for a potent humoral response. *EMBO reports*, *19*(9). https://doi.org/10.15252/embr.201846016

Meex, R. C., & Blaak, E. E. (2020). Mitochondrial dysfunction is a key pathway that links saturated fat intake to the development and progression of nafld. *Molecular Nutrition amp; Food Research*, *65*(1). https://doi.org/10.1002/mnfr.201900942

Morita, A., Hamoh, T., Perona Martinez, F. P., Chipaux, M., Sigaeva, A., Mignon, C., van der Laan, K. J., Hochstetter, A., & Schirhagl, R. (2020). The fate of lipid-coated and uncoated fluorescent nanodiamonds during cell division in yeast. *Nanomaterials*, *10*(3), 516. https://doi.org/10.3390/nano10030516

Murphy, M. P., Bayir, H., Belousov, V., Chang, C. J., Davies, K. J., Davies, M. J., Dick, T. P., Finkel, T., Forman, H. J., Janssen-Heininger, Y., & et al. (2022). Guidelines for measuring reactive oxygen species

and oxidative damage in cells and in vivo. *Nature Metabolism*, *4*(6), 651–662. https://doi.org/10.1038/s42255-022-00591-z

Mzyk, A., Sigaeva, A., & Schirhagl, R. (2022). Relaxometry with nitrogen vacancy (nv) centers in diamond. *Accounts of Chemical Research*, *55*(24), 3572–3580. https://doi.org/10.1021/acs.accounts.2c00520

Narni-Mancinelli, E., Vivier, E., & Kerdiles, Y. M. (2011). The "t-cell-ness" of nk cells: Unexpected similarities between nk cells and t cells. *International Immunology*, *23*(7), 427–431. https://doi.org/10.1093/intimm/dxr035

Niora, M., Lerche, M. H., Dufva, M., & Berg-Sørensen, K. (2023). Quantitative evaluation of the cellular uptake of nanodiamonds by monocytes and macrophages. *Small*, *19*(11). https://doi.org/10.1002/smll.202205429

Nussbaum, S. M., Krabbe, J., Boell, S., Babendreyer, A., & Martin, C. (2022). Functional changes in long-term incubated rat precision-cut lung slices. *Respiratory Research*, *23*(1). https://doi.org/10.1186/s12931-022-02169-5

Ong, S. Y., van Harmelen, R. J., Norouzi, N., Offens, F., Venema, I. M., Habibi Najafi, M. B., & Schirhagl, R. (2018). Interaction of nanodiamonds with bacteria. *Nanoscale*, *10*(36), 17117–17124. https://doi.org/10.1039/c8nr05183f

Paddock, S. W., & Eliceiri, K. W. (2013). Laser scanning confocal microscopy: History, applications, and related optical sectioning techniques. *Confocal Microscopy*, 9–47. https://doi.org/10.1007/978-1-60761-847-8_2

Patel, N. Y., Baria, D. M., Pardhi, D. S., Yagnik, S. M., Panchal, R. R., Rajput, K. N., & Raval, V. H. (2023). Microbial enzymes in pharmaceutical industry. *Biotechnology of Microbial Enzymes*, 375–403. https://doi.org/10.1016/b978-0-443-19059-9.00025-6

Perona Martinez, F. (2020). *Diamond magnetometry for sensing in biological environment.* https://doi.org/10.33612/diss.111974782

Perona Martinez, F., Nusantara, A. C., Chipaux, M., Padamati, S. K., & Schirhagl, R. (2020). Nanodiamond relaxometry-based detection of free-radical species when produced in chemical reactions in biologically relevant conditions. *ACS Sensors*, *5*(12), 3862–3869. https://doi.org/10.1021/acssensors.0c01037

Phaniendra, A., Jestadi, D. B., & Periyasamy, L. (2014). Free radicals: Properties, sources, targets, and their implication in various diseases. *Indian Journal of Clinical Biochemistry*, *30*(1), 11–26. https://doi.org/10.1007/s12291-014-0446-0

Poole, A. R., Alini, M., & Hollander, A. P. (1995). Cellular biology of cartilage degradation. *Mechanisms and Models in Rheumatoid Arthritis*, 163–204. https://doi.org/10.1016/b978-012340440-4/50041-6

Prabhakar, N., Khan, M. H., Peurla, M., Chang, H.-C., Hänninen, P. E., & Rosenholm, J. M. (2017). Intracellular trafficking of fluorescent nanodiamonds and regulation of their cellular toxicity. *ACS Omega*, *2*(6), 2689–2693. https://doi.org/10.1021/acsomega.7b00339

Rabelo, A. C., Andrade, A. K., & Costa, D. C. (2024). The role of oxidative stress in alcoholic fatty liver disease: A systematic review and meta-analysis of preclinical studies. *Nutrients*, *16*(8), 1174. https://doi.org/10.3390/nu16081174

Rasmussen, D. G., Boesby, L., Nielsen, S. H., Tepel, M., Birot, S., Karsdal, M. A., Kamper, A.-L., & Genovese, F. (2019). Collagen turnover profiles in chronic kidney disease. *Scientific Reports*, *9*(1). https://doi.org/10.1038/s41598-019-51905-3

Ray, P. D., Huang, B.-W., & Tsuji, Y. (2012). Reactive oxygen species (ros) homeostasis and redox regulation in cellular signaling. *Cellular Signalling*, *24*(5), 981–990. https://doi.org/10.1016/j.cellsig.2012.01.008

Rodriguez, A. A. (1991). Liver viability after ischemia-reperfusion. *Archives of Surgery*, *126*(6), 767. https://doi.org/10.1001/archsurg.1991.01410300113018

Rondin, L., Tetienne, J.-P., Hingant, T., Roch, J.-F., Maletinsky, P., & Jacques, V. (2014). Magnetometry with nitrogen-vacancy defects in diamond. *Reports on Progress in Physics*, *77*(5), 056503. https://doi.org/10.1088/0034-4885/77/5/056503

Sabir, U., Irfan, H. M., Alamgeer, Ullah, A., Althobaiti, Y. S., & Asim, M. H. (2022). Reduction of hepatic steatosis, oxidative stress, inflammation, ballooning and insulin resistance after therapy with safranal in nafld animal model: A new approach. *Journal of Inflammation Research*, *Volume 15*, 1293–1316. https://doi.org/10.2147/jir.s354878

Sanyal, A. J., Campbell–Sargent, C., Mirshahi, F., Rizzo, W. B., Contos, M. J., Sterling, R. K., Luketic, V. A., Shiffman, M. L., & Clore, J. N. (2001). Nonalcoholic steatohepatitis: Association of insulin resistance and mitochondrial abnormalities. *Gastroenterology*, *120*(5), 1183–1192. https://doi.org/10.1053/gast.2001.23256

Schirhagl, R., Chang, K., Loretz, M., & Degen, C. L. (2014). Nitrogen-vacancy centers in diamond: Nanoscale sensors for physics and biology. *Annual Review of Physical Chemistry*, *65*(1), 83–105. https://doi.org/10.1146/annurev-physchem-040513-103659

Seaman, S. A., Tannan, S. C., Cao, Y., Peirce, S. M., & Lin, K. Y. (2015). Differential effects of processing time and duration of collagenase digestion on human and murine fat grafts. *Plastic and Reconstructive Surgery*, *136*(2). https://doi.org/10.1097/prs.0000000000001446

Semwogerere, D., & Weeks, E. R. (2008). Confocal microscopy. In *Encyclopedia of biomaterials and biomedical engineering*. CRC Press. https://www.taylorfrancis.com/books/edit/10.1201/9780429154065/encyclopedia-biomaterials-biomedical-engineering-gary-wnek-gary-bowlin

Sharmin, R., Hamoh, T., Sigaeva, A., Mzyk, A., Damle, V. G., Morita, A., Vedelaar, T., & Schirhagl, R. (2021). Fluorescent nanodiamonds for detecting free-radical generation in real time during shear stress in human umbilical vein endothelial cells. *ACS Sensors*, *6*(12), 4349–4359. https://doi.org/10.1021/acssensors.1c01582

Shenderova, O. A., Shames, A. I., Nunn, N. A., Torelli, M. D., Vlasov, I., & Zaitsev, A. (2019). Review article: Synthesis, properties, and applications of fluorescent diamond particles. *Journal of Vacuum Science amp; Technology B, Nanotechnology and Microelectronics: Materials, Processing, Measurement, and Phenomena*, *37*(3). https://doi.org/10.1116/1.5089898

Sigaeva, A. (2022). *Fluorescent nanodiamonds as free radical sensors in live mammalian cells* [Doctoral dissertation, University of Groningen]. University of Groningen. https://doi.org/10.33612/diss.206459845

Sigaeva, A., Hochstetter, A., Bouyim, S., Chipaux, M., Stejfova, M., Cigler, P., & Schirhagl, R. (2022). Single-particle tracking and trajectory analysis of fluorescent nanodiamonds in cell-free environment and live cells. *Small*, *18*(39). https://doi.org/10.1002/smll.202201395

Sihombing, M. A., Safitri, M., Zhou, T., Wang, L., McGinty, S., Zhang, H.-J., Yin, Y., Peng, Q., Qiu, J., & Wang, G. (2021). Unexpected role of nonimmune cells: Amateur phagocytes. *DNA and Cell Biology*, *40*(2), 157–171. https://doi.org/10.1089/dna.2020.5647

Singh, S., Osna, N. A., & Kharbanda, K. K. (2017). Treatment options for alcoholic and non-alcoholic fatty liver disease: A review. *World Journal of Gastroenterology*, *23*(36), 6549–6570. https://doi.org/10.3748/wjg.v23.i36.6549

Smina, T., Mathew, J., Janardhanan, K., & Devasagayam, T. (2011). Antioxidant activity and toxicity profile of total triterpenes isolated from ganoderma lucidum (fr.) p. karst occurring in south india. *Environmental Toxicology and Pharmacology*, *32*(3), 438–446. https://doi.org/10.1016/j.etap.2011.08.011

Smirne, C., Croce, E., Di Benedetto, D., Cantaluppi, V., Comi, C., Sainaghi, P. P., Minisini, R., Grossini, E., & Pirisi, M. (2022). Oxidative stress in non-alcoholic fatty liver disease. *Livers*, *2*(1), 30–76. https://doi.org/10.3390/livers2010003

Srivastava, S. (2017). The mitochondrial basis of aging and age-related disorders. *Genes*, *8*(12), 398. https://doi.org/10.3390/genes8120398

Su, H., Cantrell, A. C., Zeng, H., Zhu, S.-H., & Chen, J.-X. (2021). Emerging role of pericytes and their secretome in the heart. *Cells*, *10*(3), 548. https://doi.org/10.3390/cells10030548

Talley, J. T., & Mohiuddin, S. S. (2023, January). *Biochemistry, fatty acid oxidation*. StatPearls Publishing.

Tanaka, S., Ohgidani, M., Hata, N., Inamine, S., Sagata, N., Shirouzu, N., Mukae, N., Suzuki, S. O., Hamasaki, H., Hatae, R., & et al. (2021). Cd206 expression in induced microglia-like cells from peripheral blood as a surrogate biomarker for the specific immune microenvironment of neurosurgical diseases including glioma. *Frontiers in Immunology*, *12*. https://doi.org/10.3389/fimmu.2021.670131

Van Overmeire, E., Laoui, D., Keirsse, J., Van Ginderachter, J. A., & Sarukhan, A. (2014). Mechanisms driving macrophage diversity and specialization in distinct tumor microenvironments and parallelisms with other tissues. *Frontiers in Immunology*, *5*. https://doi.org/10.3389/fimmu.2014.00127

Vasse, G. F., Russo, S., Barcaru, A., Oun, A. A., Dolga, A. M., van Rijn, P., Kwiatkowski, M., Govorukhina, N., Bischoff, R., & Melgert, B. N. (2023). Collagen type i alters the proteomic signature of macrophages in a collagen morphology-dependent manner. *Scientific Reports*, *13*(1). https://doi.org/10.1038/s41598-023-32715-0

Voss, B., Rauterberg, J., Allam, S., & Pott, G. (1980). Distribution of collagen type i and type iii and of two collagenous components of basement membranes in the human liver. *Pathology - Research and Practice*, *170*(1–3), 50–60. https://doi.org/10.1016/s0344-0338(80)80155-5

Wang, X., Zhang, W., Zeng, S., Wang, L., & Wang, B. (2024). Collagenase type i and probucol-loaded nanoparticles penetrate the extracellular matrix to target hepatic stellate cells for hepatic fibrosis therapy. *Acta Biomaterialia*, *175*, 262–278. https://doi.org/10.1016/j.actbio.2023.12.027

Wang, X., Luo, J., He, L., Cheng, X., Yan, G., Wang, J., & Tang, R. (2018). Hybrid ph-sensitive nanogels surface-functionalized with collagenase for enhanced tumor penetration. *Journal of Colloid and Interface Science*, *525*, 269–281. https://doi.org/10.1016/j.jcis.2018.04.084

Warraich, U.-e.-A., Hussain, F., & Kayani, H. U. (2020). Aging - oxidative stress, antioxidants and computational modeling. *Heliyon*, *6*(5). https://doi.org/10.1016/j.heliyon.2020.e04107

Wolfle, U., Seelinger, G., Bauer, G., Meinke, M. C., Lademann, J., & Schempp, C. M. (2014). Reactive molecule species and antioxidative mechanisms in normal skin and skin aging. *Skin Pharmacology and Physiology*, *27*(6), 316–332. https://doi.org/10.1159/000360092

Wong, T., Dang, K., Ladhani, S., Singal, A. K., & Wong, R. J. (2019). Prevalence of alcoholic fatty liver disease among adults in the united states, 2001-2016. *JAMA*, *321*(17), 1723. https://doi.org/10.1001/jama.2019.2276

Wright, P. B., McDonald, E., Bravo-Blas, A., Baer, H. M., Heawood, A., Bain, C. C., Mowat, A. M., Clay, S. L., Robertson, E. V., Morton, F., & et al. (2021). The mannose receptor (cd206) identifies a population of colonic macrophages in health and inflammatory bowel disease. *Scientific Reports*, *11*(1). https://doi.org/10.1038/s41598-021-98611-7

Wu, K., Vedelaar, T. A., Damle, V. G., Morita, A., Mougnaud, J., Reyes San Martin, C., Zhang, Y., van der Pol, D. P., Ende-Metselaar, H., Rodenhuis-Zybert, I., & et al. (2022). Applying nv center-based quantum sensing to study intracellular free radical response upon viral infections. *Redox Biology*, *52*, 102279. https://doi.org/10.1016/j.redox.2022.102279

Yadav, V. R., Prasad, S., Sung, B., Kannappan, R., & Aggarwal, B. B. (2010). Targeting inflammatory pathways by triterpenoids for prevention and treatment of cancer. *Toxins*, *2*(10), 2428–2466. https://doi.org/10.3390/toxins2102428

Yang, R.-L., Shi, Y.-H., Hao, G., Li, W., & Le, G.-W. (2008). Increasing oxidative stress with progressive hyperlipidemia in human: Relation between malondialdehyde and atherogenic index. *Journal of Clinical Biochemistry and Nutrition*, *43*(3), 154–158. https://doi.org/10.3164/jcbn.2008044

Yilmaz, S., Kaya, E., & Kisacam, M. A. (2017). The effect on oxidative stress of aflatoxin and protective effect of lycopene on aflatoxin damage. *Aflatoxin-Control, Analysis, Detection and Health Risks*. https://doi.org/10.5772/intechopen.69321

Zhang, Y. (2023). *Fluorescent nanodiamonds in cells: Uptake, biocompatibility and quantum sensing*. https://doi.org/10.33612/diss.797815264

Zhang, Z.-S., Zhou, H.-N., He, S.-S., Xue, M.-Y., Li, T., & Liu, L.-M. (2020). Research advances in pericyte function and their roles in diseases. *Chinese Journal of Traumatology*, *23*(2), 89–95. https://doi.org/10.1016/j.cjtee.2020.02.006

Zhou, L., Liang, Q., Li, Y., Cao, Y., Li, J., Yang, J., Liu, J., Bi, J., & Liu, Y. (2022). Collagenase-i decorated co-delivery micelles potentiate extracellular matrix degradation and hepatic stellate cell targeting for liver fibrosis therapy. *Acta Biomaterialia*, *152*, 235–254. https://doi.org/10.1016/j.actbio.2022.08.065

Zhou, Z., Xu, M.-J., & Gao, B. (2015). Hepatocytes: A key cell type for innate immunity. *Cellular amp; Molecular Immunology*, *13*(3), 301–315. https://doi.org/10.1038/cmi.2015.97